

Structure and Property Correlations in Heavy Atom Radical Conductors

Alicea A. Leitch,[†] Xueyang Yu,[‡] Stephen M. Winter,[†] Richard A. Secco,[‡]
Paul A. Dube,[§] and Richard T. Oakley*,[†]

Department of Chemistry, University of Waterloo, Waterloo, Ontario N2L 3G1, Canada,

Department of Earth Sciences, University of Western Ontario, London, Ontario N6A 5B7,
Canada, and Brockhouse Institute for Materials Science, McMaster University,
Hamilton, Ontario L8S 4L8, Canada

Received February 3, 2009; E-mail: oakley@uwaterloo.ca

Abstract: The synthesis and solid-state characterization of the resonance-stabilized heterocyclic thia/selenazyl radicals **1a–4a** is described. While all the radicals crystallize in undimerized slipped π -stacked arrays, the four crystal structures do not constitute an isomorphous set; crystals of **1a** and **3a** belong to the orthorhombic space group $P2_12_12_1$, while those of **2a** and **4a** belong to the monoclinic space group $P2_1/n$. The origin of the structural dichotomy can be traced back to the packing of the radicals in the $P2_1/n$ structure, which maximizes intermolecular Se–Se' contacts. There are marked differences in the transport properties of the two groups. Variable temperature conductivity measurements reveal high, but activated, conductivity for the monoclinic pair (**2a/4a**), with $\sigma(298\text{ K}) > 10^{-3}\text{ S cm}^{-1}$. The application of physical pressure increases the conductivity of both compounds, with $\sigma(298\text{ K})$ at 5 GPa reaching 0.5 S cm⁻¹ for **2a** and 2 S cm⁻¹ for **4a**. Variable-temperature magnetic susceptibility measurements indicate strong antiferromagnetic (AFM) coupling for the monoclinic pair **2a** and **4a**, the behavior of which has been modeled in terms of a molecular-field modified 1D Heisenberg chain of AFM coupled $S = 1/2$ centers. Extended Hückel theory band structure calculations and density functional theory first principles methods have been used to develop a qualitative understanding of the conductive and magnetic properties of radicals of the type **1–4** as a function of the degree and direction of slippage of the radical π -stacks.

Introduction

For many years the development of conductive molecular materials has relied on the use of charge transfer (CT) as the means of generating charge carriers. On the basis of this paradigm, donors such as tetrathiafulvalene and acceptors such as tetracyanoquinodimethane and C_{60} have been used to construct a host of conducting, superconducting and magnetically active salts.^{1–3} By definition, CT salts contain two components, although single-component systems can be made by incorporating donor and acceptor functions into the same

molecule.⁴ Multifunctional materials, that is, those that exhibit both conductive and magnetic behavior, have been generated by combining magnetic inorganic anions into a lattice of π -stacked organic radical cations,⁵ or by attachment of outrigger radicals (as spin polarizers) to donor molecules.⁶

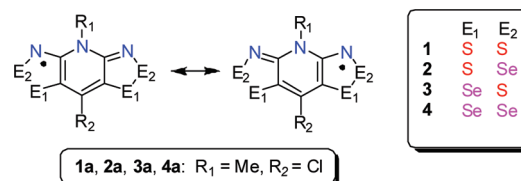
The need for charge transfer as the primary design criterion for molecular conductors can be obviated by the use of neutral radicals since, in principle at least, the unpaired electrons supplied by the radicals can serve as charge carriers.⁷ Ideally, in such materials, the radicals would behave like atoms in an elemental metal such as sodium, their mutual overlap giving

- (1) (a) Garito, A. F.; Heeger, A. J. *Acc. Chem. Res.* **1974**, *7*, 232. (b) Torrance, J. B. *Acc. Chem. Res.* **1979**, *12*, 79. (c) Williams, J. M.; Ferraro, J. R.; Thorn, R. J.; Carlson, K. D.; Geiser, U.; Wang, H. H.; Kini, A. M.; Whangbo, M.-H. *Organic Superconductors (Including Fullerenes)*; Prentice Hall: Englewood Cliffs, 1992.
- (2) (a) Bendikov, M.; Wudl, F.; Perepichka, D. *F. Chem. Rev.* **2004**, *104*, 4891. (b) Jérôme, D. *Chem. Rev.* **2004**, *104*, 5565. (c) Geiser, U.; Schlueter, J. A. *Chem. Rev.* **2004**, *104*, 5203. (d) Yamada, J.; Akutsu, H.; Nishikawa, H.; Kikuchi, K. *Chem. Rev.* **2004**, *104*, 5057. (e) Saito, G.; Yoshida, Y. *Bull. Chem. Soc. Jpn.* **2007**, *80*, 1.
- (3) (a) Haddon, R. C.; et al. *Nature* **1991**, *350*, 320. (b) Hebard, A. F.; Rosseinsky, M. J.; Haddon, R. C.; Murphy, D. W.; Glarum, S. H.; Palstra, T. T. M.; Ramirez, A. P.; Kortan, A. R. *Nature* **1991**, *350*, 600. (c) Haddon, R. C. *Acc. Chem. Res.* **1992**, *25*, 127. (d) Allemand, P. M.; Khemani, K. C.; Koch, A.; Wudl, F.; Holczer, K.; Donovan, S.; Gruner, G.; Thompson, J. D. *Science* **1991**, *253*, 301.
- (4) (a) Tanaka, H.; Okano, Y.; Kobayashi, H.; Suzuki, W.; Kobayashi, A. *Science* **2001**, *291*, 285. (b) Tanaka, H.; Tokumoto, M.; Ishibashi, S.; Graf, D.; Choi, E. S.; Brooks, J. S.; Yasuzuka, S.; Okano, Y.; Kobayashi, H.; Kobayashi, A. *J. Am. Chem. Soc.* **2004**, *126*, 10518. (c) Kobayashi, A.; Sasa, M.; Suzuki, W.; Fujiwara, E.; Tanaka, H.; Tokumoto, M.; Okano, Y.; Fujiwara, H.; Kobayashi, H. *J. Am. Chem. Soc.* **2004**, *126*, 426. (d) Kobayashi, A.; Fujiwara, E.; Kobayashi, H. *Chem. Rev.* **2004**, *104*, 5243.
- (5) (a) Coronado, E.; Galán-Mascarós, J. R.; Gómez-García, C. J.; Laukhin, V. *Nature* **2000**, *408*, 447. (b) Coronado, E.; Day, P. *Chem. Rev.* **2004**, *104*, 5419. (c) Coronado, E.; Giménez-Saiz, C.; Gómez-García, C. J. *Coord. Chem. Rev.* **2005**, *249*, 1776. (d) Coronado, E.; Giménez-Saiz, C.; Gómez-García, C.; Romero, F. M.; Tarazon, A. *J. Mater. Chem.* **2008**, *18*, 928.
- (6) (a) Matsushita, M. M.; Kawakami, H.; Kawada, Y.; Sugawara, T. *Chem. Lett.* **2007**, *110*. (b) Matsushita, M. M.; Kawakami, H.; Sugawara, T.; Ogata, M. *Phys. Rev. B* **2008**, *77*, 195208.
- (7) (a) Haddon, R. C. *Nature* **1975**, *256*, 394. (b) Haddon, R. C. *Aust. J. Chem.* **1975**, *28*, 2333. (c) Haddon, R. C. *Aust. J. Chem.* **1975**, *28*, 2343.

rise to a half-filled energy band (an $f = \frac{1}{2}$ system) and a metallic ground state. There are difficulties, however, associated with this model. First, the radicals may be subject to a Peierls distortion,⁸ which opens up an energy gap at the Fermi level and leads to a semiconducting or insulating state. A second problem arises from the high on-site Coulomb repulsion energy U associated with a half-filled energy band. If the electronic bandwidth W generated by the interaction of the radicals is insufficient to offset this on-site repulsion, which is a maximum for an $f = \frac{1}{2}$ system, the unpaired electrons become trapped on the radicals, thereby producing a Mott insulator.⁹ Overcoming these two design problems, the Peierls instability and the Mott insulating state, requires the development of radicals with highly delocalized spin distributions. Such materials resist the tendency to spin pair via σ - or π -bond formation, and are also associated with a lower on-site Coulomb potential U . To this end, research efforts have focused on highly delocalized, odd-alternant hydrocarbon radicals, specifically phenalenyls¹⁰ and spiroconjugated bis- and triphenalenyls.¹¹ Room temperature conductivities (σ_{RT}) as high as 0.3 S cm⁻¹ have been reported,^{11c} although a metallic ground state has yet to be observed.

Heteroatom radicals, notably heterocyclic thiazyls, have also been pursued as building blocks for molecular conductors.¹² In principle, the presence of a heavy heteroatom (sulfur) should provide strong intermolecular interactions, while at the same time affording more polarizable π -systems with lower U values. However, the first generations of these materials suffered from a tendency to associate, an effect which quenched the potential charge carriers.¹³ These early radicals also possessed relatively localized spin distributions so that, even when dimerization was overcome by the use of bulky substituents or at elevated

Chart 1



temperatures,^{13a,14} the resulting bandwidth was too small to offset the on-site Coulomb energy, and Mott insulating states prevailed. In pursuit of materials with a higher W/U ratio, we explored the synthesis and characterization of radicals based on the bisdithiazolyl framework **1** (Chart 1).¹⁵ Their highly delocalized spin distributions afford relatively low gas-phase disproportionation energies ΔH_{disp} and cell potentials E_{cell} ,¹⁶ indicative of a reduced on-site Coulomb energy. In addition, radicals **1** resist dimerization in the solid state, in part because of spin delocalization but also because of the buffering effect of the R₁ and R₂ groups, which prevents direct superposition and leads to slipped π -stack structures.¹⁷ However, π -stack slippage has the detrimental effect of reducing bandwidth ($W < 0.5$ eV), as a result of which conductivities remain activated, with thermal activation energies E_{act} of 0.4–0.5 eV and $\sigma(298\text{ K})$ values near 10⁻⁶ S cm⁻¹.¹⁸

Further improvements in the W/U ratio can be made by replacing sulfur with its larger, more polarizable congener selenium, to produce the mixed S/Se- and fully Se-based materials **2–4**. Early studies on derivatives of **2** (R₁ = Me, Et; R₂ = H) indicated the formation of Se–Se bonded dimers,¹⁹ a fate consistent with that of all previously studied selenazyl radicals,^{20,21} but later we showed that dimerization could be suppressed by careful choice of ligands.²² As long as dimerization can be avoided, all members of such families (**1–4**) studied to date have crystallized in isostructural sets, a feature which has allowed for a direct comparison of the effect of selenium incorporation on electronic properties. While a metallic state has not yet been achieved, it is clear that the replacement

- (8) Peierls, R. C. *Quantum Theory of Solids*; Oxford University Press: London, 1955, p 108.
- (9) (a) Mott, N. F. *Metal-Insulator Transitions*; Taylor and Francis: London, 1990. (b) Whangbo, M.-H. *J. Chem. Phys.* **1979**, *70*, 4963. (c) Friedel, J.; Noguera, C. *Int. J. Quantum Chem.* **1983**, *23*, 1209. (d) Huang, J.; Kertesz, M. *J. Phys. Chem. A* **2007**, *111*, 6304.
- (10) (a) Goto, K.; Kubo, T.; Yamamoto, K.; Nakasui, K.; Sato, K.; Shiomi, D.; Takui, T.; Kubota, M.; Kobayashi, T.; Yakusi, K.; Ouyang, J. *J. Am. Chem. Soc.* **1999**, *121*, 1619. (b) Koutentis, P. A.; Chen, Y.; Cao, Y.; Best, T. P.; Itkis, M. E.; Beer, L.; Oakley, R. T.; Brock, C. P.; Haddon, R. C. *J. Am. Chem. Soc.* **2001**, *123*, 3864. (c) Takano, Y.; Tamiguchi, T.; Isobe, H.; Kubo, T.; Morita, Y.; Yamamoto, K.; Nakasui, K.; Takui, T.; Yamaguchi, K. *J. Am. Chem. Soc.* **2002**, *124*, 11122. (d) Beer, L.; Mandal, S. K.; Reed, R. W.; Oakley, R. T.; Tham, F. S.; Donnadieu, B.; Haddon, R. C. *Cryst. Growth Des.* **2007**, *7*, 101.
- (11) (a) Chi, X.; Itkis, M. E.; Patrick, B. O.; Barclay, T. M.; Reed, R. W.; Oakley, R. T.; Cordes, A. W.; Haddon, R. C. *J. Am. Chem. Soc.* **1999**, *121*, 10395. (b) Pal, S. K.; Itkis, M. E.; Tham, F. S.; Reed, R. W.; Oakley, R. T.; Haddon, R. C. *Science* **2005**, *309*, 281. (c) Mandal, S. K.; Samanta, S.; Itkis, M. E.; Jensen, D. W.; Reed, R. W.; Oakley, R. W.; Tham, F. S.; Donnadieu, B.; Haddon, R. C. *J. Am. Chem. Soc.* **2006**, *128*, 1982. (d) Pal, S. K.; Itkis, M. E.; Tham, F. S.; Reed, R. W.; Oakley, R. T.; Haddon, R. C. *J. Am. Chem. Soc.* **2008**, *130*, 3942. (e) Haddon, R. C.; Sarkar, A.; Pal, S. K.; Chi, X.; Itkis, M. E.; Tham, F. S. *J. Am. Chem. Soc.* **2008**, *130*, 13683.
- (12) (a) Rawson, J. M.; Alberola, A.; Whalley, A. *J. Mater. Chem.* **2006**, *16*, 2560. (b) Cordes, A. W.; Haddon, R. C.; Oakley, R. T. In *The Chemistry of Inorganic Ring Systems*; Steudel, R., Ed.; Elsevier: Amsterdam, 1992; p 295. (c) Cordes, A. W.; Haddon, R. C.; Oakley, R. T. *Adv. Mater.* **1994**, *6*, 798.
- (13) (a) Andrews, M. P.; et al. *J. Am. Chem. Soc.* **1991**, *113*, 3559. (b) Cordes, A. W.; Haddon, R. C.; Hicks, R. G.; Oakley, R. T.; Palstra, T. T. M.; Schneemeyer, L. F.; Waszczak, J. V. *J. Am. Chem. Soc.* **1992**, *114*, 1729. (c) Cordes, A. W.; Haddon, R. C.; Oakley, R. T.; Schneemeyer, L. F.; Waszczak, J. A.; Young, K. M.; Zimmerman, N. M. *J. Am. Chem. Soc.* **1991**, *113*, 582. (d) Bryan, C. D.; Cordes, A. W.; Haddon, R. C.; Glarum, S. H.; Hicks, R. G.; Kennepohl, D. K.; MacKinnon, C. D.; Oakley, R. T.; Palstra, T. T. M.; Perel, A. S.; Schneemeyer, L. F.; Scott, S. R.; Waszczak, J. V. *J. Am. Chem. Soc.* **1994**, *116*, 1205.
- (14) (a) Beekman, R. A.; Boeré, R. T.; Moock, K. H.; Parvez, M. *Can. J. Chem.* **1998**, *76*, 85. (b) Banister, A. J.; Bricklebank, N.; Clegg, W.; Elsegood, M. R. J.; Gregory, C. I.; Lavender, I.; Rawson, J. M.; Tanner, B. K. *J. Chem. Soc., Chem. Commun.* **1995**, 679. (c) Banister, A. J.; Bricklebank, N.; Lavender, I.; Rawson, J. M.; Gregory, C. I.; Tanner, B. K.; Clegg, W.; Elsegood, M. R. J.; Palacio, F. *Angew. Chem., Int. Ed. Engl.* **1996**, *35*, 2533.
- (15) (a) Beer, L.; Brusso, J. L.; Cordes, A. W.; Haddon, R. C.; Itkis, M. E.; Kirschbaum, K.; MacGregor, D. S.; Oakley, R. T.; Pinkerton, A. A.; Reed, R. W. *J. Am. Chem. Soc.* **2002**, *124*, 9498. (b) Cordes, A. W.; Haddon, R. C.; Oakley, R. T. *Phosphorus, Sulfur, Silicon Rel. Elem.* **2004**, *179*, 673.
- (16) ΔH_{disp} is the enthalpy change for the conversion of two gas-phase radicals R into a cation/anion pair, i.e., $2\text{R} \rightleftharpoons \text{R}^+ + \text{R}^-$, and is equal to the difference between the ionization potential (IP) and electron affinity (EA). The cell potential $E_{\text{cell}} = E_{1/2(\text{ox})} - E_{1/2(\text{red})}$ is the difference between the half-wave potentials for the oxidation and reduction processes.
- (17) In the absence of an R₂ substituent the radicals are susceptible to dimerization: Leitch, A. A.; McKenzie, C. E.; Oakley, R. T.; Reed, R. W.; Richardson, J. F.; Sawyer, L. D. *Chem. Commun.* **2006**, 1088.
- (18) (a) Beer, L.; Brusso, J. L.; Cordes, A. W.; Haddon, R. C.; Godde, I.; Itkis, M. E.; Oakley, R. T.; Reed, R. W. *Chem. Commun.* **2002**, 2562. (b) Beer, L.; Britten, J. F.; Brusso, J. L.; Cordes, A. W.; Haddon, R. C.; Itkis, M. E.; MacGregor, D. S.; Oakley, R. T.; Reed, R. W.; Robertson, C. M. *J. Am. Chem. Soc.* **2003**, *125*, 14394. (c) Beer, L.; Britten, J. F.; Clements, O. P.; Haddon, R. C.; Itkis, M. E.; Matkovich, K. M.; Oakley, R. T.; Reed, R. W. *Chem. Mater.* **2004**, *16*, 1564.
- (19) Beer, L.; Brusso, J. L.; Haddon, R. C.; Itkis, M. E.; Kleinke, H.; Leitch, A. A.; Oakley, R. T.; Reed, R. W.; Richardson, J. F.; Secco, R. A.; Yu, X. *J. Am. Chem. Soc.* **2005**, *127*, 1815.

of sulfur by selenium leads to improved conductivities and lower activation energies. What has also emerged from these explorations is the realization that the heavier heteroatom selenium enhances not only charge transport but also magnetic exchange interactions. Radicals **3** and **4** ($R_1 = \text{Et}$, $R_2 = \text{H}$), for example, undergo phase transitions to spin-canted antiferromagnetic states with ordering temperatures of 18 and 27 K respectively,²³ while **2** and **4** ($R_1 = \text{Et}$, $R_2 = \text{Cl}$) order as bulk ferromagnets with T_c values of 12.8 and 17.0 K.^{24,25} These ordering temperatures are among the highest ever observed for nonmetal-based ferromagnetic materials.

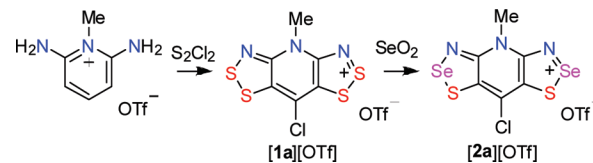
In the present work we describe the preparation and solid-state characterization of the family of radicals **1–4** ($R_1 = \text{Me}$, $R_2 = \text{Cl}$), hereafter referred to as **1a–4a**, as in Chart 1. While association is avoided for all four radicals, their solid-state structures do not form an isostructural set. Instead, the crystal structures separate into two pairs belonging to the space groups $P_{2}1_2_1_2_1$ (**1a**, **3a**) and $P_{2}1/n$ (**2a**, **4a**). This dichotomy has provided a unique opportunity to study the dependence of magnetic and transport properties on crystal packing. Variable-temperature conductivity and magnetic susceptibility measurements indicate higher conductivity and stronger antiferromagnetic (AFM) interactions for the monoclinic pair. The latter can be modeled in terms of a molecular-field modified 1D Heisenberg chain of AFM coupled $S = 1/2$ centers. Variations in the conductivity and magnetic properties of radicals of the type **1–4** as a function of the degree and direction of slippage of the radical π -stacks have been probed by means of extended Hückel theory (EHT) band calculations and density functional theory (DFT) methods.

Results

Synthesis. Preparative routes to salts of the all-sulfur framework **1a** are well documented.¹⁸ The most straightforward of these is based on a double Herz cyclization of *N*-methyl-2,6-

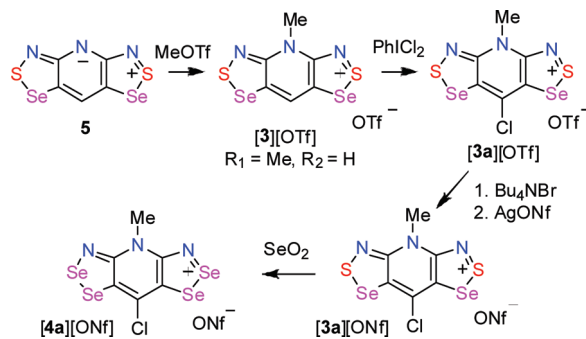
- (20) (a) Cordes, A. W.; Haddon, R. C.; Oakley, R. T.; Schneemeyer, L. F.; Waszczak, J. V.; Young, K. M.; Zimmerman, N. M. *J. Am. Chem. Soc.* **1991**, *113*, 582. (b) Andrews, M. P.; et al. *J. Am. Chem. Soc.* **1991**, *113*, 3559. (c) Cordes, A. W.; Haddon, R. C.; Hicks, R. G.; Oakley, R. T.; Palstra, T. T. M.; Schneemeyer, L. F.; Waszczak, J. V. *J. Am. Chem. Soc.* **1992**, *114*, 1729. (d) Britten, J. F.; Clements, O. P.; Cordes, A. W.; Haddon, R. C.; Oakley, R. T.; Richardson, J. F. *Inorg. Chem.* **2001**, *40*, 6820. (e) Beer, L.; Cordes, A. W.; Myles, D. J. T.; Oakley, R. T.; Taylor, N. J. *CrysEngChem* **2000**, *2*, 109. (f) Oakley, R. T.; Reed, R. W.; Cordes, A. W.; Craig, S. L.; Graham, S. B. *J. Am. Chem. Soc.* **1987**, *109*, 7745. (g) Bryan, C. D.; Cordes, A. W.; Oakley, R. T.; Spence, R.E.v., H. *Acta Crystallogr. C* **1995**, *51*, 2402. (h) Cordes, A. W.; Glarum, S. H.; Haddon, R. C.; Hallford, R.; Hicks, R. G.; Kennepohl, D. K.; Oakley, R. T.; Palstra, T. T. M.; Scott, S. R. *J. Chem. Soc., Chem. Commun.* **1992**, 1265.
- (21) (a) Feeder, N.; Less, R. J.; Rawson, J. M.; Oliete, P.; Palacio, F. *Chem. Commun.* **2000**, 2449. (b) Parvez, M.; Boeré, R. T. *Acta Crystallogr., Sect. C* **1995**, *51*, 2118.
- (22) (a) Beer, L.; Brusso, J. L.; Haddon, R. C.; Itkis, M. E.; Leitch, A. A.; Oakley, R. T.; Reed, R. W.; Richardson, J. F. *Chem. Commun.* **2005**, 1543. (b) Brusso, J. L.; Cvrljaj, K.; Leitch, A. A.; Oakley, R. T.; Reed, R. W.; Robertson, C. M. *J. Am. Chem. Soc.* **2006**, *128*, 15080. (c) Brusso, J. L.; Derakhshan, S.; Itkis, M. E.; Kleinke, H.; Haddon, R. C.; Oakley, R. T.; Reed, R. W.; Richardson, J. F.; Robertson, C. M.; Thompson, L. K. *Inorg. Chem.* **2006**, *45*, 10958.
- (23) Leitch, A. A.; Brusso, J. L.; Cvrljaj, K.; Reed, R. W.; Robertson, C. M.; Dube, P. A.; Oakley, R. T. *Chem. Commun.* **2007**, 3368.
- (24) (a) Robertson, C. M.; Myles, D. J. T.; Leitch, A. A.; Reed, R. W.; Dooley, D. M.; Frank, N. L.; Dube, P. A.; Thompson, L. K.; Oakley, R. T. *J. Am. Chem. Soc.* **2007**, *129*, 12688. (b) Robertson, C. M.; Leitch, A. A.; Cvrljaj, K.; Reed, R. W.; Myles, D. J. T.; Dube, P. A.; Oakley, R. T. *J. Am. Chem. Soc.* **2008**, *130*, 8414.
- (25) Robertson, C. M.; Leitch, A. A.; Cvrljaj, K.; Myles, D. J. T.; Reed, R. W.; Dube, P. A.; Oakley, R. T. *J. Am. Chem. Soc.* **2008**, *130*, 14791.

Scheme 1



diaminopyridinium triflate (trifluoromethanesulfonate = OTf^-) with sulfur monochloride (Scheme 1), which affords **[1a][OTf]** in a single step. Incorporation of selenium into the 2-position to yield **[2a][OTf]** was initially accomplished by heating **[1a][OTf]** with selenium dioxide in acetic acid (HOAc). This method, first developed²⁶ for the introduction of selenium into simple 1,2,3-dithiazolylium salts,²⁷ is fast and proceeds in high yield, but the incorporation is not always regiospecific.²⁵ Greater specificity was obtained by performing the reaction in acetonitrile (MeCN) at 110°C in a pressure vessel. Progress of the insertion was monitored by mass spectrometry, with complete conversion to (>99%) S_2Se_2 material being achieved in about 72 h.

Scheme 2



Access to salts of the *N*-methylated cations **[3a]⁺** and **[4a]⁺** was achieved using the procedure developed for the corresponding *N*-ethylated materials (Scheme 2),²⁴ beginning with the methylation of zwitterion **5** to afford **[3][OTf]** ($R_1 = \text{Me}$, $R_2 = \text{H}$). Treatment of the latter with iodobenzene dichloride produced the desired chlorinated derivative **[3a][OTf]**. Attempts to introduce selenium into this material by metathesis with SeO_2 were thwarted by the low solubility of **[4a][OTf]** in MeCN . However, when the triflate anion was replaced with nonaflate (nonafluorobutanesulfonate, ONF^-), selenium insertion proceeded smoothly in MeCN at 110°C (in a pressure vessel) to give **[4a][ONF]**. This salt displayed sufficient solubility in acetonitrile for purification by crystallization and subsequent chemical and electrochemical reduction experiments.

Reduction of the salts of **[2a][OTf]**, **[3a][OTf]**, and **[4a][ONF]** to the respective radicals could be effected using chemical or, in one case, electrochemical methods. We considered a variety of reducing agents, including deca-, octa- and hexamethylferrocene (DMFc, OMFc and HMFc respectively), tetrakisdimethylaminoethylene (TDAE) and *N,N,N',N'*-tetramethyl-*p*-phenylenediamine (TMMPDA). The choice of reductant was dictated in part by the reduction potentials of the cations, estimated from the known values of the recently reported *N*-Et

- (26) Akulin, Y. I.; Gel'mont, M. M.; Strelets, B.; Efros, L. S. *Khim. Geterotsikl. Soedin.* **1978**, 912.
- (27) A similar approach has been used to incorporate selenium into dithiadiazolylum salts. For example, see: Less, R. J.; Rawson, J. M.; Jones, M. *Polyhedron* **2001**, *20*, 523.

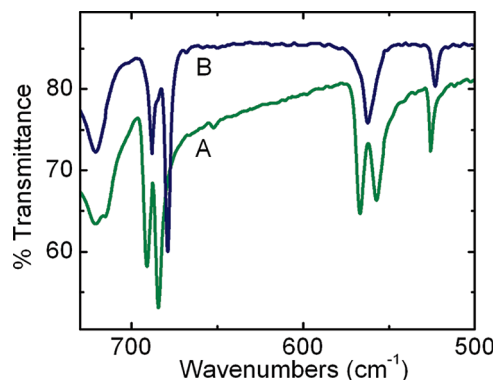


Figure 1. FTIR spectrum of **4a** produced by electrochemical (A) and TMPDA (B) reduction.

series,²⁴ and partly by concerns about potential contamination of the resulting radicals by paramagnetic byproducts, notably ferrocinium salts. Thus, while HMFc was effective in providing single crystals of **2a** and **3a** suitable for X-ray work, we turned to the use of TMPDA for the generation of bulk material for magnetic and conductivity measurements. In the case of **2a**, the phase purity of the material produced using TMPDA was confirmed by powder X-ray diffraction, which also established that the structure was identical to that determined from single crystal measurements (*vide infra*).

Reduction of **[4a][ONf]** to **4a** was not so straightforward. Infrared and powder X-ray analysis of bulk radical generated by chemical reduction with TDAE, OMFc and TMPDA suggested the formation of at least two phases, the relative abundance of which depended on the reducing agent. Single-phase material could, however, be produced by electroreduction of **[4a][ONf]**. While only small quantities (5–10 mg) of radical could be made from a 48 h reduction at 10 μ A, sufficient material could eventually be prepared for both single-crystal structure determination and bulk physical (conductivity and magnetic) measurements. All electrochemically grown samples were checked for phase purity by infrared analysis. Figure 1 illustrates the fingerprint region of the infrared spectrum of **4a** produced by electrochemical reduction, as well as a sample of **4a** prepared by chemical reduction with TMPDA. The latter material consists almost exclusively of a different, as yet unidentified phase.

Crystal Structures. One of the four radicals under consideration, the all-sulfur material **1a**, was structurally characterized as part of an earlier study. Its crystal structure belongs to the orthorhombic space group $P2_12_12_1$ and consists of slipped π -stacks of undimerized radicals.^{15a} In keeping with previous trends,^{23,24} structural analysis on **3a** confirmed that replacement of sulfur in the 1-position by selenium occurs with retention of both space group and packing pattern. To our surprise, however, crystallographic analysis of the two remaining radicals **2a** and **4a** (the latter produced electrochemically) provided something completely different. While these two structures also consist of slipped π -stack arrays of undimerized radicals, and are themselves isostructural, there is no correspondence between this pair of compounds and the other two members of the series. Instead, crystals of **2a** and **4a** belong to the monoclinic space group $P2_1/n$. Crystal data for all four radicals are listed in Table 1, and selected intra- and intermolecular metrics for the two pairs are presented in Tables 2 and 3. ORTEP drawings of the four radicals are illustrated in Figure 2, and representative views of the unit cells of **2a** and **3a** are shown in Figures 3 and 4,

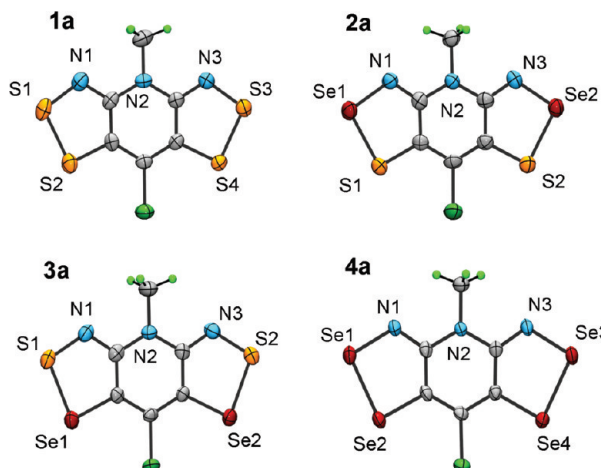


Figure 2. ORTEP drawings (50% thermal ellipsoids) of **1a**–**4a**, with atom numbering.

respectively. Also illustrated in Figures 3 and 4 are the slipped π -stack motifs and intermolecular chalcogen–chalcogen contacts for **2a** and **3a**. Differences in the lateral slippage of the two groups of radicals along the π -stacks are illustrated in Figure 5, which shows adjacent pairs viewed perpendicular to their mean molecular planes. The translation coordinates x and y of one radical relative to the next are listed in Tables 2 and 3, as are values of δ , the mean plate-to-plate separation of the radicals along the π -stacks.

While there is no indication in the crystal structures of radical dimerization in either a σ - or π -mode, there are numerous close intermolecular interactions which influence the magnetic and conductive properties of the materials. These interactions, classified in terms of the S/Se contacts $d1$ – $d5$ for **1a**/**3a** and $r1$ – $r5$ for **2a**/**4a**, all fall close to or within the van der Waals separation²⁸ for the appropriate combination of S and Se centers.²⁹ In the orthorhombic structures (**1a**/**3a**) the packing of the radical π -stacks produces two columns related by a 2-fold screw axis and linked by the contacts $d3$ and $d4$. Two other π -stacks act as pincers via contacts $d1$, $d2$ and $d5$ on either side of the first two. In the monoclinic systems **2a**/**4a** the crystal packing affords interpenetrating slipped π -stacks linked across an inversion center by the contact $r3$. The orientation of the two remaining π -stacks generates a cross-braced effect, the intersection of the stacks affording the contacts $r1$, $r2$ and $r4$. In addition to these interstack contacts, all of which are Se–Se', slippage of the π -stacks in **2a**/**4a** is such that there is a close intrastack contact $r5$, the particular importance of which, on magnetic and conductive properties, is evaluated in the following sections.

Band Structures. In order to explore the electronic structures of the four radicals **1a**–**4a** we have carried out a series of EHT band structure calculations on the crystal structure geometries. The results must be viewed with caution, as the tight-binding approximation is unable to provide a proper description of the ground state of strongly correlated systems such as those reported here. These shortcomings notwithstanding, the method provides qualitative insight into the direction and extent of intermolecular orbital interactions within and between radical

(28) (a) Bondi, A. *J. Phys. Chem.* **1964**, *68*, 441. (b) Dance, I. *New J. Chem.* **2003**, *27*, 22.

(29) The following van der Waals separations were taken from reference 28a: S–S', 3.6; S–Se', 3.7; Se–Se', 3.8 Å.

Table 1. Crystallographic Data

	1a ^a	2a	3a	4a
formula	C ₆ H ₃ ClN ₃ S ₄	C ₆ H ₃ ClN ₃ S ₂ Se ₂	C ₆ H ₃ ClN ₃ S ₂ Se ₂	C ₆ H ₃ ClN ₃ Se ₄
M	280.8	374.6	374.60	468.4
a (Å)	4.2464(12)	4.1566(4)	4.1932(2)	4.1978(2)
b (Å)	15.194(5)	14.0039(12)	15.1413(8)	14.3180(8)
c (Å)	15.069(4)	16.4888(15)	16.1531(8)	16.7655(9)
β (deg)	90	94.338(6)	90	96.2200(10)
V (Å ³)	972.2(5)	957.04(15)	1025.57(9)	1001.74(9)
ρ_{calcd} (g cm ⁻³)	1.918	2.600	2.426	3.106
space group	P2 ₁ 2 ₁ 2 ₁	P2 ₁ /n	P2 ₁ 2 ₁ 2 ₁	P2 ₁ /n
Z	4	4	4	4
temp (K)	293(2)	295(2)	295(2)	296(2)
μ (mm ⁻¹)	1.208	15.983	7.836	14.873
λ (Å)	0.71073	1.54178	0.71073	0.71073
data/restr./parameters	1915/0/128	1661/0/127	2760/0/127	2050/0/128
solution method	direct methods	direct methods	direct methods	direct methods
R, R_w (on F^2)	0.0314, 0.0544	0.0442, 0.1035	0.0268, 0.0499	0.0235, 0.0521

^a Data from reference 15a.**Table 2.** Selected Metrics for 1a and 3a at Ambient Temperature

	1a ^a ($E_1 = S$)	3a ($E_1 = Se$)
N–S (Å)	1.657(3), 1.664(3)	1.652(3), 1.660(3)
S–E ₁ (Å)	2.0981(15), 2.1046(15)	2.2381(9), 2.2462(9)
E ₁ –C (Å)	1.727(4), 1.735(4)	1.860(3), 1.883(3)
C–C (Å)	1.437(5), 1.438(5)	1.427(4), 1.440(4)
C–N (Å)	1.300(5), 1.305(4)	1.311(4), 1.312(4)
d1 (Å)	3.541(2)	3.424(1)
d2 (Å)	3.324(2)	3.430(1)
d3 (Å)	3.369(2)	3.473(1)
d4 (Å)	3.546(2)	3.572(1)
d5 (Å)	3.861(2)	3.698(1)
δ (Å)	3.470(5)	3.500(1)
x, y (Å) ^b	2.45, 0.07 ^c	2.31, 0.11
deviation from mean plane (Å)	0.0252	0.0373

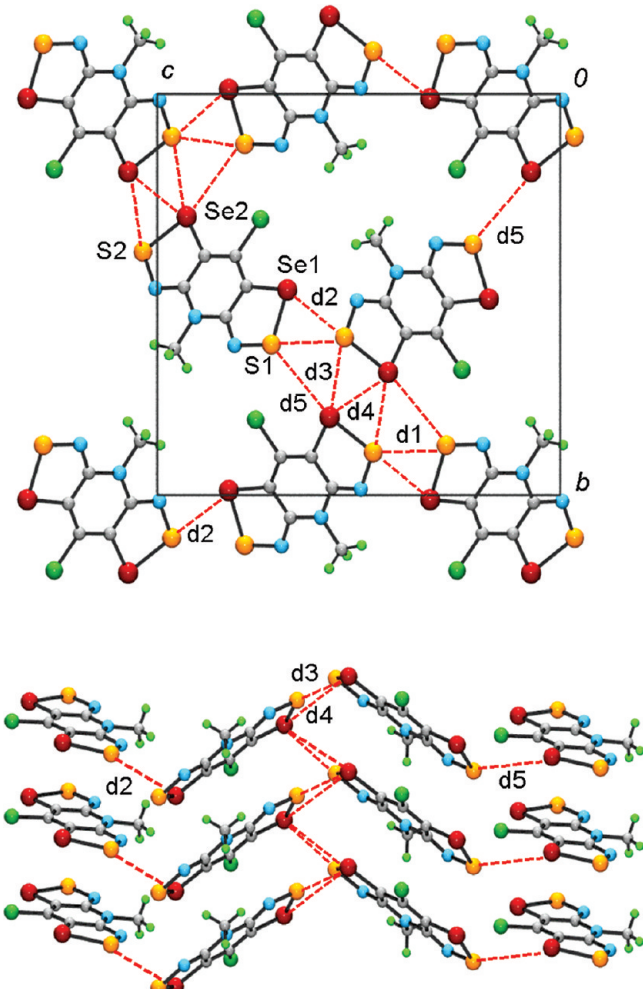
^a Data from reference 15a. ^b Slippage coordinates defined in Figure 5.^c At 25 K, x = 2.99, y = 0.03 Å.**Table 3.** Selected Metrics for 2a and 4a at Ambient Temperature

	2a ($E_1 = S$)	4a ($E_1 = Se$)
N–Se (Å)	1.839(6), 1.822(6)	1.826(3), 1.816(3)
Se–E ₁ (Å)	2.241(2), 2.250(2)	2.3591(5), 2.3646(5)
C–E ₁ (Å)	1.736(7), 1.743(7)	1.877(3), 1.874(3)
C–C (Å)	1.441(9), 1.454(9)	1.434(4), 1.438(4)
C–N (Å)	1.294(9), 1.298(8)	1.305(4), 1.311(4)
r1 (Å)	3.273(1)	3.313(1)
r2 (Å)	3.390(1)	3.449(1)
r3 (Å)	3.525(1)	3.509(1)
r4 (Å)	3.677(1)	3.700(1)
r5 (Å)	3.687(2)	3.746(1)
δ (Å)	3.517(1)	3.568(1)
x, y (Å) ^a	1.60, 1.54	1.49, 1.64
deviation from mean plane (Å)	0.0463	0.0445

^a Slippage coordinates defined in Figure 5.

π -stacks across the entire series. The results are presented in terms of the electronic bandwidth W , expressed here in terms of the dispersion energy $\Delta E_k = [E_{(k=\pi/a)} - E_{(k=0)}]$ of the crystal orbitals (COs) under consideration; within this context $W = |\Delta E_k|$.

Previous work on the EHT band structures of radicals of the type **1–4** have focused on the dispersion of the crystal orbitals arising from interactions between the singly occupied molecular orbitals (SOMOs)³⁰ in the relevant unit cells. Regardless of the choice of chalcogen (E = S or Se) and the nature of the R₁/R₂ ligands, this a_2 symmetry orbital (Figure 6) consists of an out-

**Figure 3.** Unit cell drawing of 3a (above), showing intermolecular contacts d1–d5 (Table 2), and slipped π -stack architecture (below).

of-phase combination of the SOMOs associated with two five-membered dithiazolyl rings. It possesses a nodal plane through the central pyridine ring which, to first order, suppresses the

(30) A DFT description of the a_2 symmetry singly occupied molecular orbital of **1** (R₁ = H, R₂ = Cl) is provided in ref 19. Within a family of radicals **1–4** the SOMOs all display the same nodal features, regardless of the nature of the chalcogen.

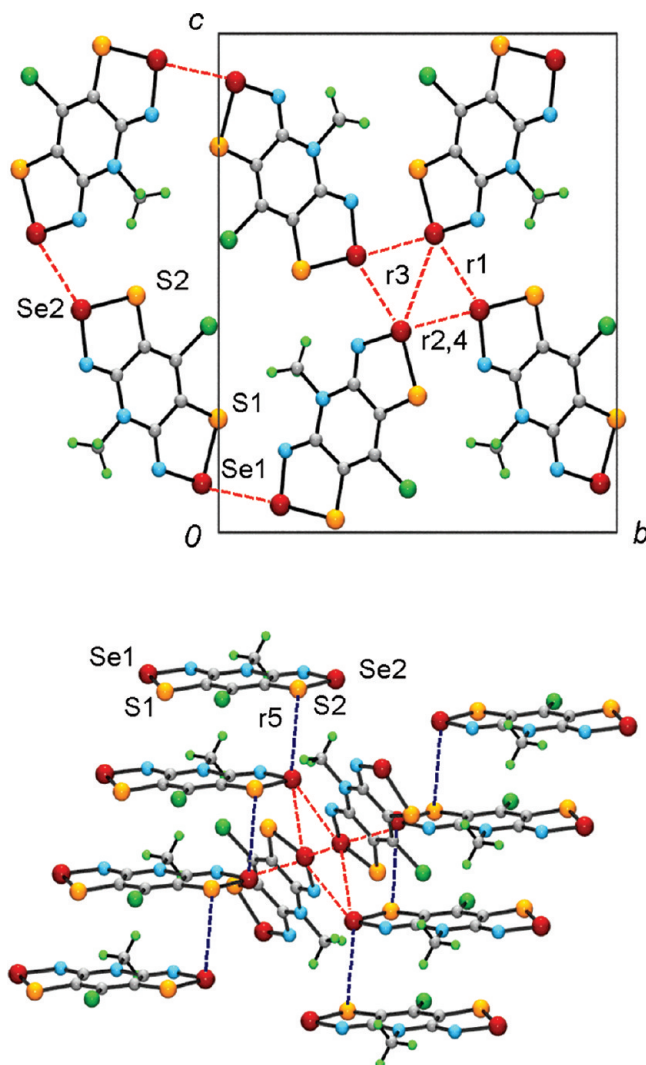


Figure 4. Unit cell drawing of **2a** (above), showing intermolecular S/Se contacts r_1 – r_4 (Table 3), and interpenetrating slipped π -stack architecture (below), with plate-to-plate contact r_5 .

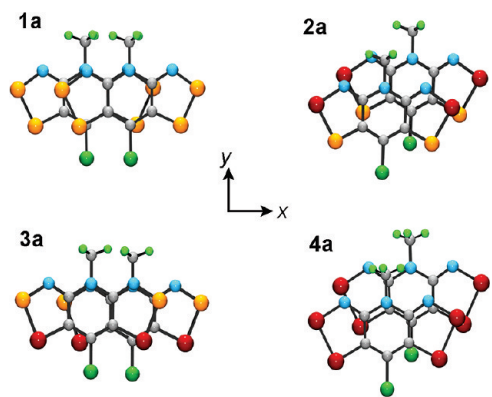


Figure 5. Slippage of π -stacks of **1a**–**4a**, and translational coordinates x and y .

electronic effects of the R_1/R_2 ligands. It is also antibonding over the E–E, E–C and E–N bonds, a feature which gives rise to significant but not easily anticipated changes in intermolecular overlap, and hence CO dispersion, as a function of stack slippage. This potential for variations in dispersion energy with slippage is clearly demonstrated in the EHT band structures

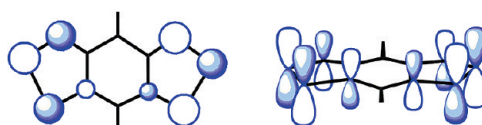


Figure 6. Idealized views of the SOMO for **1**–**4** ($E = S/Se$).

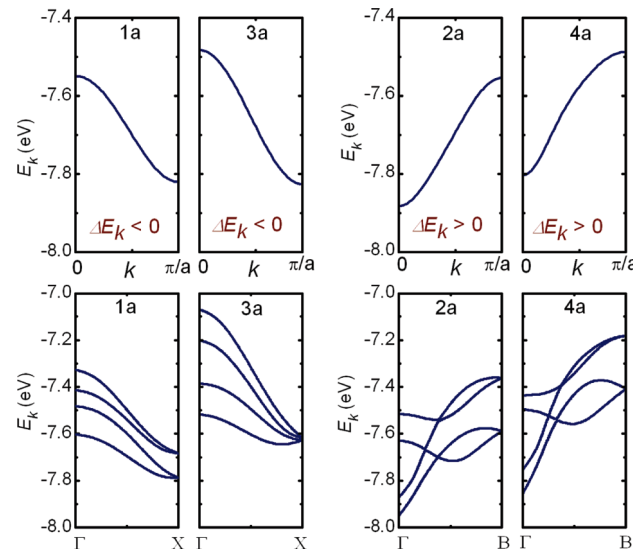


Figure 7. EHT crystal orbital dispersion curves (1D above and 3D below) for **1a**–**4a**.

of **1a**/**3a** and **2a**/**4a** shown in Figure 7. When the calculations are restricted to a single 1D π -stack, a single CO corresponding to the radical SOMO is observed, while in the full 3D structure there are four COs, arising from the four SOMOs in the respective unit cells, to consider.³¹ Both sets of calculations (1D and 3D) afford the same conclusion, that there is an inversion of the dispersion energy curves between **1a**/**3a** ($\Delta E_k < 0$) and **2a**/**4a** ($\Delta E_k > 0$), an effect that arises from a change in intermolecular overlap between neighboring radicals along the π -stack. It is also apparent, from the energetic spread of the four COs, that lateral interstack interactions are extensive in both pairs of compounds, that is, the electronic structures are relatively three-dimensional (3D). Indeed the contribution to the total bandwidth from divergence of the four COs is approximately the same as that which stems from the largest dispersion of a single CO. Overall the 3D bandwidth W increases slightly with selenium content, as expected, with the two mixed S/Se compounds displaying approximately the same value of W .

While the difference in the slopes of the dispersion curves is readily evident in both the 1D and 3D band structures, the origin of the effect is, as noted above, less obvious. As illustrated in Figure 5 slippage of the radicals in **1a**/**3a** is along the x direction, while in **2a**/**4a** the molecular plates move along both x and y . Based on the sign of ΔE_k , it would appear that the overall intermolecular overlap $S_{(k=0)}$ between two SOMOs in **1a**/**3a** is negative (antibonding), while for **2a**/**4a** it is positive (bonding). In the case of **1a**/**3a**, this outcome is hard to anticipate simply by inspection of individual interatomic interactions (Figure 8),

(31) In the full cell calculations the COs are plotted along the reciprocal space directions Γ (0,0,0) to X (1/2,0,0) for **1a**/**3a** and Γ (0,0,0) to B (1/2,0,0) for **2a**/**4a**. Dispersion along these reciprocal space vectors can be associated precisely (for $P_{2_1}2_1$) and approximately (for P_{2_1}/n) with orbital interactions along the stacking axis in real space.

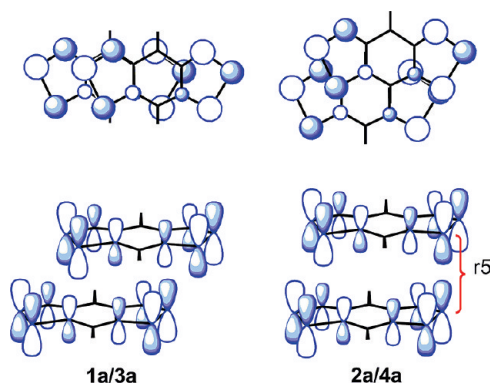


Figure 8. Overlap of adjacent SOMOs in **1a/3a** and **2a/4a** viewed from above and side.

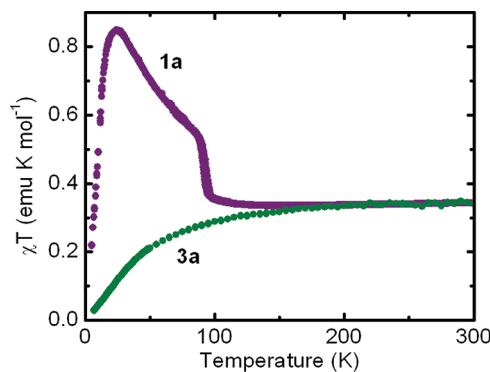


Figure 9. Plots of χT versus T for **1a** and **3a**.

Table 4. Conductivity and Magnetic Parameters

	1a ^b	2a	3a	4a
W (eV)	0.46 (0.27) ^c	0.58 (0.34) ^c	0.59 (0.33) ^c	0.68 (0.32) ^c
$\sigma(298\text{ K})$ (S cm^{-1}) ^a	5.3×10^{-6}	2.1×10^{-3}	3.5×10^{-5}	4.3×10^{-3}
E_{act} (eV) ^a	0.395	0.20	0.30	0.17
C (emu K mol ⁻¹)	0.357	—	0.378	—
θ (K)	-13	—	-28	—
J (cm ⁻¹) ^d	—	-101	—	-64
zJ (cm ⁻¹) ^d	—	-17	—	-49

^a Data from ambient pressure measurements. ^b Data from reference 15a. ^c Numbers in parentheses are from 1D single π -stack calculations.

^d Parameters extracted using a molecular-field modified Bonner–Fisher 1D $S = 1/2$ AFM coupled chain model.

but in the case of **2a/4a** the net positive overlap can be ascribed to the importance of the interaction of the almost perfectly aligned $p\pi$ -orbitals on adjacent S/Se (**2a**) or Se/Se (**4a**) atoms along the stack (contact *r5*). Other, more general implications of plate slippage in π -stacked radicals of this type on overlap, bandwidth and magnetic exchange are discussed below.

Magnetic Measurements. Early magnetic susceptibility χ measurements as a function of temperature on the orthorhombic radical **1a** established that the material behaved as a Curie–Weiss paramagnet at temperatures above 100 K (Figure 9).^{15a} Values of C and θ obtained from a Curie–Weiss fit to the high-temperature data are provided in Table 4. Just below 100 K the structure was observed to undergo a first-order phase transition, which was established crystallographically to involve a small but abrupt increase in plate slippage (vide infra). This process was accompanied by a slightly hysteretic increase in χT with decrease in T which signaled the onset of local ferromagnetic (FM) interactions. At lower temperatures this surge was

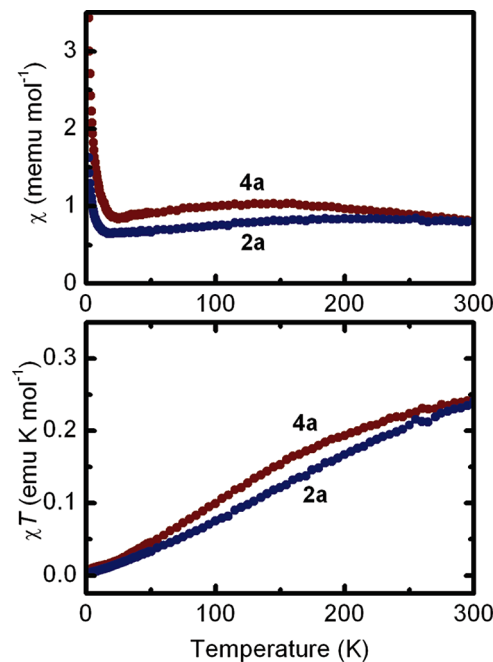


Figure 10. Plots of χ versus T (above) and χT versus T (below) for **2a** and **4a**.

overcome by weaker antiferromagnetic (AFM) effects. We have now carried out magnetic measurements on the isostructural selenium radical **3a**, the results of which are presented in Figure 9 in the form of a plot of χT (χ corrected for diamagnetic contributions) versus T . There is no indication of the structural phase change seen for **1a**. Instead the material behaves as a weakly antiferromagnetically coupled paramagnet from 7–300 K. There is a very slight discontinuity in the $\chi(T)$ vs T plot (at 100 Oe) near 7 K which may indicate the onset of spin-canted AFM ordering. The high temperature ($T > 100$ K) data could nonetheless be fitted to the Curie–Weiss expression to afford a C -value of 0.378 emu K mol⁻¹ and Weiss constant of -28 K.

The magnetic behavior of the two monoclinic radicals **2a** and **4a** is markedly different from that of the orthorhombic pair described above. Plots of χ versus T and χT versus T for both compounds (Figure 10) indicate the effects of much stronger antiferromagnetic exchange interactions, the value of χT never reaching (up to 300 K) the value of 0.375 emu K mol⁻¹ expected for an $S = 1/2$ paramagnet. No attempt was made to force the magnetic data for **2a** and **4a** into the Curie–Weiss expression. Instead, the results were analyzed in terms of a 1D Heisenberg chain of AFM coupled $S = 1/2$ centers. This approach was prompted in part from the stacking observed for **2a** and **4a** (Figure 4), which affords strong intermolecular S/Se (in **2a**) and Se/Se (in **4a**) overlap through the *r5* contact, an alignment that might be expected to give rise to a strong AFM exchange interaction. Similar effects have been observed in π -stacked bisthiadiazinyls.³² The exchange parameters derived from fits based on a molecular-field modified Bonner–Fisher approach³³ and Heisenberg Hamiltonian $H_{\text{ex}} = -2J\{S_1 \cdot S_2\}$ are listed in

(32) Leitch, A. A.; Oakley, R. T.; Reed, R. W.; Thompson, L. K. *Inorg. Chem.* **2007**, *46*, 6261.

(33) Bonner, J. C.; Fisher, M. E. *Phys. Rev. A* **1964**, *135*, 640.

Table 4.³⁴ While reasonable correlations were achieved in both cases, it is apparent from the large zJ values for **2a** and, more particularly, **4a** that lateral magnetic interactions are strong, and that the molecular-field modified 1D chain is at best a first approximation to the description of their magnetic structures.³⁵

In order to explore the origin of the strong AFM interactions in **2a** and **4a**, and the appropriateness of a 1D chain model to fit the magnetic data, we have explored the local magnetic exchange interactions along the π -stacks. We have used an abbreviated first principles approach,³⁶ within which bulk magnetic properties are represented as a composite of the individual exchange interactions arising from all pairwise combinations of a radical and its nearest neighbors in the lattice. The method, which has been successfully applied to a variety of nitrogen-centered radicals,³⁷ heterocyclic thiazyls,^{38,39} selenazyls and phenalenyls,⁴⁰ employs exchange energies estimated from broken symmetry DFT methods pioneered by Noddleman.⁴¹ Accordingly, and with reference to the formal Hamiltonian $H_{\text{ex}} = -2J\{S_1 \cdot S_2\}$, the exchange energy J for any pair of interacting radicals can be estimated from the total energies of the triplet (E_{TS}) and broken symmetry singlet (E_{BSS}) states and the respective expectation values $\langle S^2 \rangle$, according to eq 1.

$$J = \frac{-(E_{\text{TS}} - E_{\text{BSS}})}{\langle S^2 \rangle_{\text{TS}} - \langle S^2 \rangle_{\text{BSS}}} \quad (1)$$

There are many pairwise combinations possible between the radical π -stacks of **2a** and **4a**, all of which are illustrated in Figure 11. In addition to exchange interactions along the π -stacks, denoted here as J_{π} , there are a total of seven lateral interstack interactions for every radical. However, six of these fall into symmetry related pairs J_1 , J_2 and J_4 , while the seventh, J_3 , which links radicals in an end-to-end fashion across an inversion center, is unique. Single-point total energies E_{TS} and E_{BSS} were calculated for these five combinations (J_1-J_4 , J_{π}) using the hybrid exchange correlation functional UB3LYP and a series of polarized, split-valence basis sets with double- ζ (6-31G(d,p)) and triple- ζ (6-311G(d,p)) functions.

Calculated values for the exchange energies J_1-J_4 and J_{π} for **2a** and **4a** are listed in Table 5. While there are minor differences between the two basis sets, it is clear that the large AFM

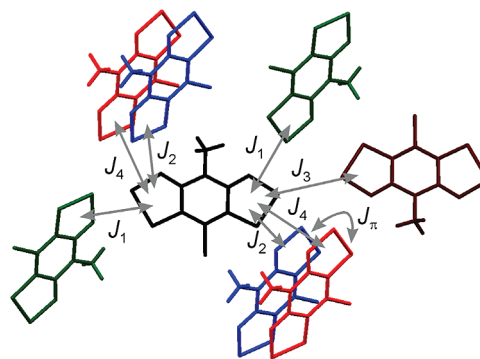


Figure 11. Pairwise exchange interactions J_1-J_4 and J_{π} .

Table 5. Calculated (UB3LYP) π -Stack Exchange Coupling Energies^a

	2a		4a	
	6-31G(d,p)	6-311G(d,p)	6-31G(d,p)	6-311G(d,p)
J_1	3.62	3.73	5.33	5.35
J_2	5.13	5.20	4.39	4.37
J_3	-13.77	-15.4	-14.24	-16.03
J_4	3.20	2.83	5.14	5.05
J_{π}	-100.18	-97.5	-68.94	-65.78

^a J -values in cm^{-1} calculated from eq 1 using single-point electronic energies.

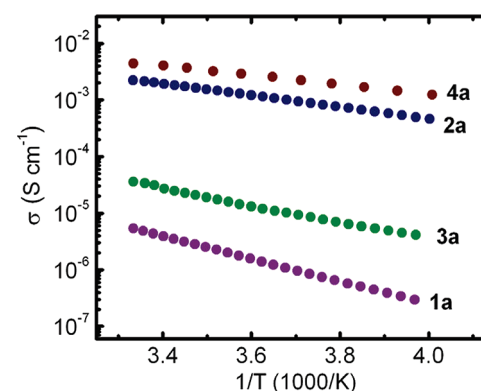


Figure 12. Log plot of σ versus $1/T$ for **1a/3a** ($P_2\text{I}_2\text{I}_1$) and **2a/4a** ($P_2\text{I}_n$).

- (34) The exchange equation was modified to include a molecular field correction, which suggested a large secondary AFM term, zJ . Full details of the fits for **2a** and **4a** are provided in the Supporting Information.
- (35) Given the magnitude of the single lateral exchange interaction J_3 , a spin ladder description could also be used. See, for example: Rovira, C. *Struct. Bonding (Berlin)* **2001**, *100*, 164.
- (36) Deumal, M.; Robb, M. A.; Novoa, J. J. *Prog. Theor. Chem. Phys.* **2007**, *16*, 271.
- (37) (a) Novoa, J. J.; Deumal, M. *Struct. Bonding (Berlin)* **2001**, *100*, 33. (b) Jornet, J.; Deumal, M.; Ribas-Ariño, J.; Bearpark, M. J.; Robb, M. A.; Hicks, R. G.; Novoa, J. J. *Chem.-Eur. J.* **2006**, *12*, 3995.
- (38) (a) Rawson, J. M.; Luzon, J.; Palacio, F. *Coord. Chem. Rev.* **2005**, *249*, 2631. (b) Luzon, J.; Campo, J.; Palacio, F.; McIntyre, G. J.; Rawson, J. M. *Polyhedron* **2005**, *24*, 2579. (c) Deumal, M.; LeRoux, S.; Rawson, J. M.; Robb, M. A.; Novoa, J. J. *Polyhedron* **2007**, *26*, 1949. (d) Jornet, J.; Robb, M. A.; Deumal, M.; Novoa, J. J. *Inorg. Chim. Acta* **2008**, *361*, 3586.
- (39) (a) Decken, A.; Mattar, S. M.; Passmore, J.; Shubaev, K. V.; Thompson, L. K. *Inorg. Chem.* **2006**, *45*, 3878. (b) Leitch, A. A.; Oakley, R. T.; Reed, R. W.; Thompson, L. K. *Inorg. Chem.* **2007**, *46*, 6261.
- (40) Takano, Y.; Taniguchi, T.; Isobe, H.; Kubo, T.; Morita, Y.; Yamamoto, K.; Nakasui, K.; Takui, T.; Yamaguchi, K. *J. Am. Chem. Soc.* **2002**, *124*, 11122.
- (41) (a) Noddleman, L.; Norman, J. G. *J. Chem. Phys.* **1979**, *70*, 4903. (b) Noddleman, L. *J. Chem. Phys.* **1981**, *74*, 5737.

(negative) intrastack exchange energy J_{π} dominates. The lateral interstack interactions are, by comparison, much smaller, the effects of the FM set J_1 , J_2 and J_4 being offset by the single larger AFM term J_3 . Collectively, the results provide qualitative support for interpreting the magnetic data in terms of a molecular-field modified 1D Heisenberg chain model, although they do not preclude other interpretations.³⁵

Conductivity Measurements. Variable-temperature four-probe conductivity measurements have been performed on the three selenium-based radicals **2a**, **3a** and **4a**. The results are presented in Figure 12, which shows log plots of the conductivity (σ) as a function of inverse temperature (along with data obtained previously for **1a**).^{15a} Derived activation energies ΔE_{act} , along with values of $\sigma(298 \text{ K})$ are provided in Table 4. The results reflect those seen for **1–4** ($R_1 = \text{Et}$, $R_2 = \text{Cl}$)²⁴ and elsewhere,^{22,23} in that conductivities are enhanced, and activation energies reduced, by the incorporation of selenium in place of sulfur. It is also clear, however, that the performance of the materials can be distinguished by structure type, that is, there is a marked difference in the properties of **1a/3a** and **2a/4a**, the

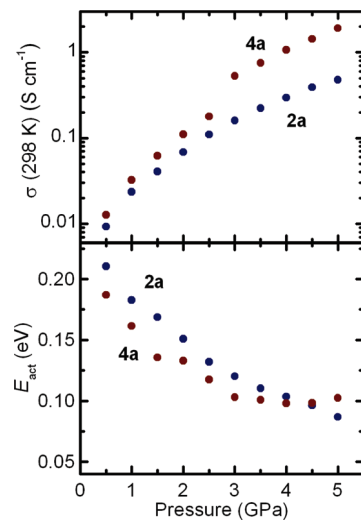


Figure 13. Plots of σ (298 K) (above) and E_{act} (below) versus applied pressure for **2a/4a**.

conductivity values of the monoclinic pair being much higher than that of the orthorhombic set. Indeed the values of σ (298 K) for **2a/4a** are the highest we have seen for any thiazyl or selenazyl radical conductor.

Given the high conductivity of **2a/4a** we have explored the effect of physical pressure on the conductivity of these two radicals using a cubic anvil press. The results are summarized in Figure 13, which shows plots of conductivity and thermal activation energy as a function of applied pressure over the range 0–5 GPa. As observed in previous pressure studies on thiazyl/selenazyl radicals,⁴² compression of the crystal structure leads to a shortening of the intermolecular contacts and a concomitant increase in bandwidth, a process which, in turn, increases conductivity. For both compounds, the response is strong, with σ (298 K) increasing by two orders of magnitude at 5 GPa and reaching, in the case of **4a**, a value of 2 S cm⁻¹. There is also a substantial reduction in the activation energy. This decrease is relatively linear with pressure for **2a**, with E_{act} falling to near 0.08 eV at 5 GPa, while for **4a** the decrease appears to level off at a plateau value near 0.10 eV. The origin of this difference in the pressure dependence of the activation energy of the two compounds was, at first, surprising. In view of its higher selenium content, we had anticipated that **4a** would respond more dramatically than **2a** under pressure. The apparent anomaly may reflect a lower and perhaps less isotropic⁴³ compressibility for **4a**, an effect which can be related to the buffering effect of the lateral noncovalent interactions, that is, those interactions which do not contribute to solid-state electronic bandwidth but rather inhibit the compression of the crystal structure. To illustrate this point we show in Figure 14 a cluster of four radicals of **2a** and the nonbonding intermolecular S–Me' (*b*1, *b*2), S–Cl' (*b*3) and Cl–Cl' (*b*4) contacts that separate them. Specific distances, along with those corresponding to the analogous interactions in **4a**, are also listed. All these contacts are close to or inside the respective van der Waals separations,⁴⁴ and as a result, compression of the structures will have to work against the combined buffering effect of these interactions. In

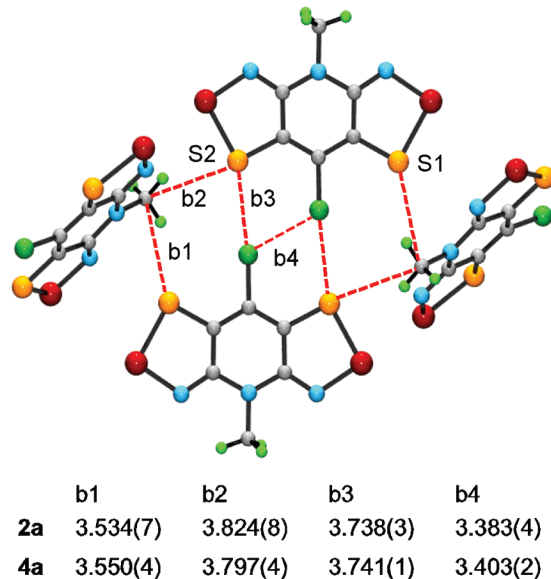


Figure 14. Buffering interactions *b*1–*b*4 (in Å) for **2a** (and **4a**).

the case of **4a**, where Se–Me' and Se–Cl' contacts (with larger van der Waals separations) are involved, compression energies are likely to be larger. These issues notwithstanding, it is apparent that at 5 GPa the metallic state is not far removed for either compound and may be accessible by increased physical pressure or by small structural modifications (chemical pressure).

Discussion

The search for single-component conductive materials based on neutral radicals has been predicated on the need for materials in which dimerization is suppressed, so that the unpaired electrons are available to serve as charge carriers. The second, and perhaps more challenging design criterion, has been to overcome the high on-site Coulomb repulsion energy *U* associated with an *f* = 1/2 system. If the bandwidth *W* could be made sufficiently large to offset *U*, so as to afford a metallic state, the electronic structures would be well described by band theory.⁹ At the other extreme, that is, in strongly correlated, low bandwidth (*W* ≪ *U*) systems where Mott insulating states prevail, a Heitler–London valence bond model provides a better description. For intermediate systems such as the quasi-1D π-stacked structures **2a/4a**, where high but not metallic conductivity is observed, and symmetry breaking effects of a Peierls distortion are resisted, the Anderson 1D resonating valence bond (RVB) model⁴⁵ may be used,^{11b,c} or the Hubbard Hamiltonian can be employed.⁴⁶ In the latter case the 1D half-filled band is related to the Heisenberg linear chain by the relationship $|J| = 2t^2/U$,⁴⁷ where *J* is the Bonner–Fisher exchange interaction and

- (42) Beer, L.; Brusso, J. L.; Haddon, R. C.; Itkis, M. E.; Oakley, R. T.; Reed, R. W.; Richardson, J. F.; Secco, R. A.; Yu, X. *Chem. Commun.* **2005**, 5745.
 (43) Espallargas, G. M.; Brammer, L.; Allan, D. R.; Pulham, C. R.; Robertson, N.; Warren, J. E. *J. Am. Chem. Soc.* **2008**, 130, 9058.

- (44) The following van der Waals separations apply: S–Me', 3.80; S–Cl', 3.55; Cl–Cl', 3.50; Se–Me', 3.90; Se–Cl', 3.65 Å. This information was compiled from data in ref 28a as well as from: (a) Dougill, M. W.; Paddock, N. L. *J. Chem. Soc., Dalton Trans.* **1974**, 1022. (b) Brant, D. A.; Miller, W. G.; Flory, P. J. *J. Mol. Biol.* **1967**, 23, 47. (c) Brant, D. A.; Flory, P. J. *J. Am. Chem. Soc.* **1965**, 87, 2791.
 (45) (a) Anderson, P. W. *Phys. Rev.* **1952**, 86, 694. (b) Anderson, P. W. *Mater. Res. Bull.* **1973**, 8, 153. (c) Anderson, P. W.; Lee, P. A.; Randeria, M.; Rice, T. M.; Trivedi, N.; Zhang, F. C. *J. Phys.: Condens. Matter* **2004**, 16, R755.
 (46) (a) Anderson, P. W. *Science* **1987**, 235, 1196. (b) Cho, A. *Science* **2006**, 314, 1072.
 (47) (a) Ovchinnikov, A. A. *Sov. Phys. JETP Lett.* **1970**, 30, 1160. (b) Shiba, H.; Pincus, P. A. *Phys Rev. B* **1972**, 5, 1966.

t is the charge transfer (resonance) integral ($4t = W$). For **2a/4a** a 1D designation is probably an oversimplification, but if we assume such a model holds, and set $U \approx 0.8$ V (from electrochemical data) and $W \approx 0.33$ eV (from the 1D single π -stack band calculations), then $|J| = 2t^2/U \approx 0.017$ eV or near 140 cm^{-1} , a value broadly consistent with the experimentally derived J_π -values.

However, while debate over the best electronic description of these nearly metallic materials continues, the challenge from a synthetic perspective is to anticipate what modifications, such as changes in R_1/R_2 , could be made to radicals of the type **1–4** in order to improve their conductive and magnetic properties. Over the past few years we have reported the crystal structures of a variety of derivatives and have attempted, on a case-by-case basis, to correlate structure and property. For the highly conductive and strongly antiferromagnetic materials **2a/4a** described here, a combination of EHT and DFT methods have allowed us to identify the pathway for charge transport and the principal contributor (J_π) to the intermolecular magnetic exchange energy. However, what is lacking in this analysis is a comprehensive view of the electronic and magnetic interactions possible for these radicals as a function of structure. Are there other geometries based on the slipped π -stack motif that might afford better performance?

In order to explore this possibility, and hence provide a guide for future work, we have performed a series of calculations of the electronic and magnetic interactions within a single radical π -stack as a function of the degree of radical slippage. To simplify the number of variables we constructed a set of model radicals **1–4** ($R_1 = R_2 = H$) with idealized molecular geometries taken from C_{2v} optimized UB3LYP/6-31G(d,p) calculations. Each of these models was then used as the building block for a series of (i) EHT calculations of the 1D π -SOMO dispersion energy ΔE_k and (ii) DFT (UB3LYP/6-31G(d,p)) calculations of the pairwise intrastack exchange energy J_π .⁴⁸ Both series of calculations considered the effects of all possible translations (slippage) along x and y ,⁴⁹ using an interplanar separation (δ) of 3.5 \AA . Some special cases illustrated in Figure 15 include direct superposition, hereafter expressed as [0.0, 0.0], and extreme slippage along the x axis [3.0, 0.0], the y axis [0.0, 3.0] and both axes [3.0, 3.0].

Analysis and interpretation of the results of these calculations is best accomplished with reference to energy surface plots as a function of x and y . To this end we illustrate in Figures 16 and 17 the EHT 1D dispersion energy ΔE_k ⁵⁰ and magnetic exchange energy J_π surfaces for **1** and **4** ($R_1 = R_2 = H$); these two models are qualitatively representative of the other two structures (**3** and **2** respectively).⁵¹ While there are subtle differences between the two dispersion plots and between the two exchange energy plots, the surface topologies within each pair are similar, as a result of which we focus first on correlating the differences between the ΔE_k and J_π surfaces. Ideally, one would like to be able to develop such a comparison in the light of the well-established relationship between the overlap of magnetically active orbitals and the sign and magnitude of

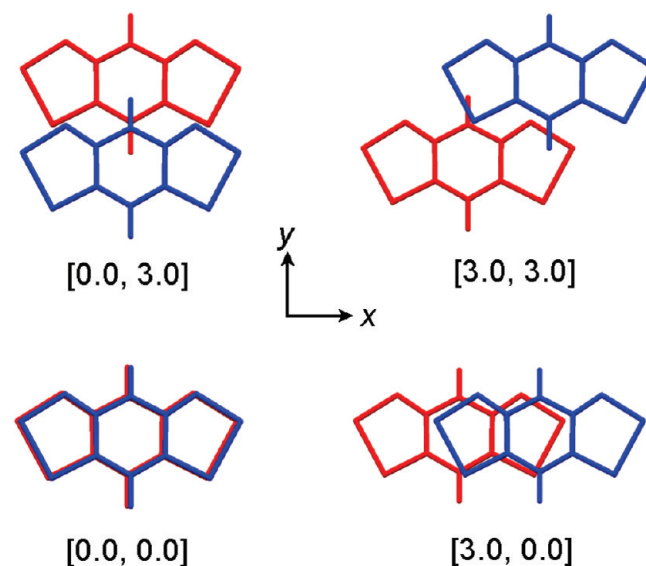


Figure 15. Slippage of π -stacks of model radicals **1–4** ($R_1 = R_2 = H$) as a function of x and y .

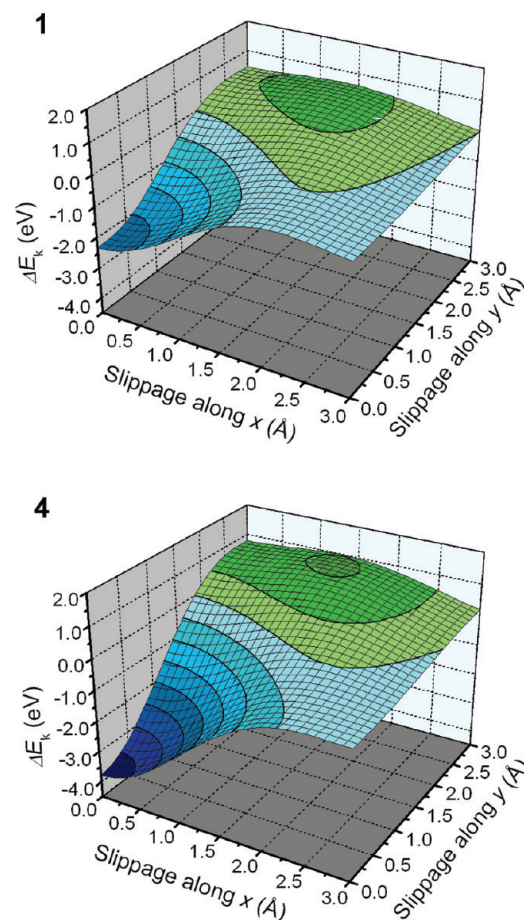


Figure 16. Surface plots of ΔE_k (eV) as a function of x and y for **1** and **4** ($R_1 = R_2 = H$) with $\delta = 3.5\text{ \AA}$. Contour lines are drawn at intervals of 0.5 eV.

- (48) Similar approaches for developing magneto-structural correlations have been used elsewhere. See, for example: Ribas-Arino, J.; Novoa, J. J.; Miller, J. S. *J. Mater. Chem.* **2006**, *16*, 2600.
- (49) For the model structures, with $R_1 = R_2 = H$, translations along $\pm x$ and $\pm y$ are equivalent by symmetry.
- (50) The overall bandwidth $W = |\Delta E_k|$. As illustrated in Figure 7, a positive value of S at $k = 0$ gives rise to a positive ΔE_k , and vice versa.
- (51) Contour plots of ΔE_k and J_π for all four models **1–4** ($R_1 = R_2 = H$) are provided in the Supporting Information.

magnetic exchange effects arising therefrom.⁵² Accordingly, antiferromagnetic effects would be expected to dominate the value of J_π in those regions where absolute overlap, expressed here in terms of $|\Delta E_k|$, is large. Conversely, the contribution of ferromagnetic effects to the value of J_π should be maximized wherever there is orthogonal overlap, that is, where $|\Delta E_k| = 0$.

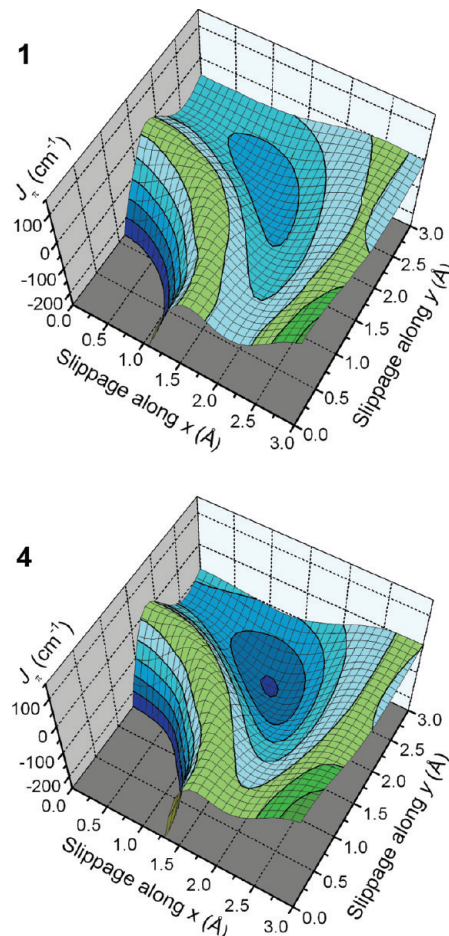


Figure 17. Surface plots of J_{π} (cm^{-1}) as a function of x and y for **1** and **4** ($R_1 = R_2 = \text{H}$) with $\delta = 3.5 \text{ \AA}$. Contour lines are drawn at intervals of 50 cm^{-1} .

The major features of the energy surfaces are readily correlated within this context. Thus, when the radical π -stacks are directly superimposed, at $[0.0, 0.0]$, intermolecular overlap is expected to be strong ($S_{(k=0)} \ll 0$), and certainly $|\Delta E_k|$ is large in this region. Concomitantly, J_{π} sinks into a deep and computationally unfathomed⁵³ antiferromagnetic ($J_{\pi} \ll 0$) “hole” in this region. As the stacks slip away from direct superposition along either the x or y directions, the bandwidth $|\Delta E_k|$ decreases and J_{π} becomes less antiferromagnetic. Continued slippage eventually leads to an orthogonal overlap condition ($|\Delta E_k| = 0$), beyond which bandwidth increases and antiferromagnetic effects reassert their influence on the value of J_{π} . Thus, the broad local maximum in $|\Delta E_k|$ near $[1.5, 2.5]$ is matched on the J_{π} maps by the development of a wide antiferromagnetic “lagoon”. Separating the two regions of strong overlap (large $|\Delta E_k|$) is, as noted earlier, a contour line of zero bandwidth. Using orbital orthogonality arguments one might expect to see the emergence of ferromagnetic exchange interactions in this region and, satisfactorily, the $\Delta E_k = 0$ contour line in Figure 16 tracks

(52) (a) Kahn, O. *Molecular Magnetism*; VCH: New York, 1993. (b) Kahn, O.; Briat, B. *J. Chem. Soc., Faraday Trans.* **1976**, 2, 268. (c) Kahn, O.; Galy, J.; Journaux, Y.; Jaud, J.; Morgenstern-Badarau, I. *J. Am. Chem. Soc.* **1982**, 104, 2165. (d) Verdaguer, M. *Polyhedron* **2001**, 20, 1115. (e) Fujita, W.; Kikuchi, K. *Chem. Asian. J.* **2009**, 4, 400.

(53) We were unable to achieve convergence on a broken symmetry singlet state ($\langle S^2 \rangle = 1$) for slippage coordinates close to the origin $[0.0, 0.0]$. Attempts to do so always resulted in a closed shell singlet ($\langle S^2 \rangle = 0$), that is, a π -dimer.

remarkably close to the (green) ferromagnetic “ridge” enclosed by the $J_{\pi} = 0$ contours in Figure 17. In addition to this ridge, there is an “island” of strong ferromagnetic exchange near $[3.0, 0.0]$ which, in the case of **4**, rises to a maximum value of $J_{\pi} > 100 \text{ cm}^{-1}$. The relevance of this feature is discussed below.

The trends in $|\Delta E_k|$ and J_{π} across the series **1–4** ($R_1 = R_2 = \text{H}$) provide a satisfying demonstration of the effect of selenium incorporation on bandwidth and exchange energy. For example, sequential replacement of sulfur by selenium increases intermolecular overlap, leading to a steady rise in the limiting bandwidth $|\Delta E_k|$ at $[0.0, 0.0]$ along the series **1** ($2.30 \text{ eV} < \mathbf{2}$ ($3.18 \text{ eV} \approx \mathbf{3}$ ($3.15 \text{ eV} < \mathbf{4}$ (3.77 eV)). Likewise the magnitude of the local maximum in $|\Delta E_k|$ near $[1.5, 2.5]$ follows a similar trend, one which correlates with the increase in depth of the antiferromagnetic J_{π} lagoon found in the same region. In addition to the changes arising from the extent of selenium content, both the ΔE_k and J_{π} maps reveal differences associated with the position of selenium incorporation. For example, in the case of **1** (and **3**) the AFM lagoon centered around $[1.5, 2.5]$ extends to and reaches the x -axis, emerging as an AFM channel at $y = 0$ across the region $1.6 < x < 2.4$. By contrast, in **4** (and **2**) the effect of AFM interactions is less extensive, so that J_{π} remains positive along the entire x axis. Essentially, the AFM well in **4** (and **2**) is deeper, but more localized.

Several conclusions can be drawn from the results of these model calculations. First, for heavy atom radicals such as those reported here, the pursuit of directly superimposed radical π -stacks is unlikely to be successful, as the SOMO–SOMO interactions are so strong. While high bandwidths can be anticipated, the predicted exchange energies are strongly antiferromagnetic. Overall, the trends in overlap and exchange energy go hand-in-hand, each heralding the energetic preference for a singlet π -dimer. In accord with this conclusion, our attempts to generate superimposed bisdithiazolyl π -stacks have inevitably led to structures possessing a diamagnetic ground state.⁵⁴ Preservation of an undimerized radical in the solid state must, we believe, involve the use of a slipped π -stack motif. Accordingly, the challenge becomes one of designing radicals in which stack slippage affords reasonable bandwidths. The above calculations suggest that such configurations are theoretically possible, for example near $[1.5, 2.5]$, but can they be made?

In partial response to this question we consider the conductivity and magnetic properties of the radicals **1a–4a** in terms of their slippage coordinates and the relationship of these to the model 1D bandwidth and J_{π} energy surfaces. In the orthorhombic pair slippage occurs exclusively along x , to afford coordinates of **1a** [2.45, 0.07] and **3a** [2.31, 0.11]. Inspection of Figure 16 places these materials in a region of relatively low 1D-bandwidth, as a result of which high conductivity is neither expected nor observed. At the same time, exchange interactions J_{π} are predicted (Figure 17) to be weak. It is therefore not surprising that both materials display relatively small (negative) Weiss constants (Table 4). Interestingly, the ferromagnetic surge^{15a} which accompanies the phase change of **1a** (Figure 9) now finds a ready explanation in terms of the J_{π} map, as the slippage coordinates [2.99, 0.03] of the low-temperature phase move the material well onto the ferromagnetic island around $[3.0, 0.0]$ noted above. The slippage coordinates of the monoclinic radicals **2a** [1.60, 1.54] and **4a** [1.49, 1.64] are markedly different from those of the orthorhombic pair, in that they place

(54) Leitch, A. A.; Reed, R. W.; Robertson, C. M.; Britten, J. F.; Yu, X.; Secco, R. A.; Oakley, R. T. *J. Am. Chem. Soc.* **2007**, 129, 7903.

the radicals in a region of strong positive overlap. While the resulting bandwidths $|\Delta E_k|$ are smaller than those predicted for the ideal maxima near [1.5, 2.5], they are sufficiently large to provide the best conductivities we have observed for an $f = 1/2$ system. At the same time the large, negative J_π values observed and calculated for these two radicals can be seen as a simple consequence of their general location on the steep downward slope leading into the AFM lagoon near [1.5, 2.5]. It would therefore appear that the variations in electronic and magnetic properties with structure of the slipped π -stack radicals **1a–4a** can be qualitatively correlated with the locations of the radicals on the model 1D EHT bandwidth and DFT exchange energy surface maps. To this extent, it is appealing to consider modifications to **2a/4a**, that is, changes in R_1 and R_2 , that are sufficiently small to preserve the space group and crystal packing and sufficiently large to move the stack slippage closer to the high bandwidth zone.

Summary and Conclusions

Compounds **1a–4a** represent the first set of mixed S/Se heterocyclic radicals to display nonisomorphous crystal structures. While dimerization has been suppressed across the entire series, two different packing patterns are observed, each giving rise to distinct transport properties. The interpenetrating slipped π -stack motif adopted by **2a** and **4a** allows for strong intrastack chalcogen-chalcogen interactions which enhance both bandwidth and antiferromagnetic exchange interactions. The room temperature conductivities $\sigma(298\text{ K})$ for this pair are both greater than 10^{-3} S cm^{-1} and represent, to our knowledge, the highest ever observed for nominally $f = 1/2$ systems. Moreover, $\sigma(298\text{ K})$ can be increased by the application of physical pressure to afford, in the case of **4a**, a value of 2 S cm^{-1} at 5 GPa. While the conductivity remains activated, the low activation energy suggests that metallic conductivity, even superconductivity, is not far removed, and may be accessible with slightly increased physical pressures ($>5\text{ GPa}$).⁵⁵ Alternatively, minor structural modifications (changes in R_1/R_2) may afford the necessary “chemical pressure” to ease the structures closer to more favorable bandwidths.

In an attempt to correlate the crystal structures of radicals of the general type **1–4** with bulk property, that is, conductivity and magnetism, we have performed calculations of the EHT bandwidths and DFT exchange energies associated with model 1D arrays of π -stacked radicals **1–4** ($R_1 = R_2 = \text{H}$) as a function of stack slippage. The resulting energy surfaces have provided qualitative insight into the structural motifs which are conducive to enhanced intrastack overlap, and hence conductivity, as well as those that give rise to strong ferromagnetic and antiferromagnetic exchange along the π -stack. These structure/property correlations will, we believe, facilitate the design of materials with improved charge transport and magnetic properties.

Experimental Section

General Procedures and Starting Materials. The reagents selenium dioxide, Proton Sponge, methyl triflate, tetra-*n*-butylammonium bromide, silver nonafluorobutanesulfonate (nonaflate, ONF^-), hexamethylferrocene (HMFC), and *N,N,N',N'*-tetramethyl-*p*-phenylenediamine (TMPDA) were obtained commercially. Com-

(55) (a) Takabayashi, Y.; Ganin, A. Y.; Jegliè, P.; Arèon, D.; Takano, T.; Iwasa, Y.; Ohishi, Y.; Takata, M.; Takeshita, N.; Prassides, K.; Rosseinsky, M. J. *Science* **2009**, 323, 1585. (b) Tosatti, E. *Science* **2009**, 323, 1570.

pound [**1a**][OTf],^{15a} zwitterion **5**^{24b} and iodobenzene dichloride⁵⁶ were prepared according to literature methods. HMFC was purified by sublimation in vacuo and recrystallization from acetonitrile, and TMPDA was purified by sublimation in vacuo. The solvents acetonitrile (MeCN), dichloroethane (DCE), acetic acid (HOAc), and dichloromethane (DCM) were of at least reagent grade. MeCN was dried by distillation from P_2O_5 and/or CaH_2 , and both DCE and DCM by distillation from P_2O_5 . All reactions were performed under an atmosphere of dry nitrogen. Infrared spectra (Nujol mulls, KBr optics) were recorded on a Nicolet Avatar FTIR spectrometer at 2 cm^{-1} resolution. ^1H spectra were run on a Bruker Avance 300 MHz NMR spectrometer and low-resolution electro-spray ionization (ESI) mass spectra were run on a Micromass Q-TOF Ultima Global LC/MS/MS system. Elemental analyses were performed by MHW Laboratories, Phoenix, AZ 85018.

8-Chloro-4-methyl-4H-bis[1,2,3]thiaselenazolo[4,5-b:5',4'-e]pyridin-2-iun Triflate [**2a**][OTf]. Compound [**1a**][OTf] (0.859 g, 2.00 mmol) and finely ground selenium dioxide (0.666 g, 6.00 mmol) were combined with 80 mL of MeCN in a glass pressure vessel which was heated at 110 °C for 3 days in an oil bath. The reaction mixture was hot filtered on a glass Büchner funnel and the filtrate concentrated to 50 mL. After 16 h the red-brown solid of [**2a**][OTf] was filtered off and washed with 10 mL of MeCN, yield 0.740 g (1.41 mmol, 71%). Recrystallization from MeCN afforded red needles, dec >292 °C. IR: 1419 (s), 1397 (m), 1353 (m), 1341 (m), 1280 (s), 1230 (s), 1170 (s), 1152 (m), 1048 (w), 1022 (s), 977 (m), 855 (w), 749 (s), 636 (s), 594 (s), 584 (s), 543 (w), 514 (m), 478 (w) cm^{-1} . Anal. Calcd for $\text{C}_7\text{H}_3\text{ClF}_3\text{N}_3\text{O}_3\text{S}_3\text{Se}_2$: C, 16.05; H, 0.58; N, 8.02%. Found: C, 16.27; H, 0.44; N, 8.19%.

Preparation of 4-Methyl-4H-bis[1,2,3]selenathiazolo[4,5-b:5',4'-e]pyridin-2-iun Triflate, [**3a**][OTf] ($\text{R}_1 = \text{Me}$, $\text{R}_2 = \text{H}$). Methyl triflate (3.40 mL, 30.0 mmol) was added to a solution of Proton Sponge (1.31 g, 6.11 mmol) dissolved in 200 mL of DCE. Compound **5** (3.95 g, 12.1 mmol) was added and after 16 h the red solid of [**3a**][OTf] ($\text{R}_1 = \text{Me}$, $\text{R}_2 = \text{H}$) was filtered off and washed 3 × with 80 mL of DCE, yield 5.48 g (11.2 mmol, 92%). The product was purified by double recrystallization from MeCN and isolated as red needles, dec >233 °C. IR: 1529 (w), 1497 (w), 1352 (s), 1270 (s), 1242 (s), 1224 (s), 1156 (s), 1033 (s), 1015 (m), 903 (m), 858 (m), 831 (m), 759 (w), 731 (s), 713 (m), 684 (s), 655 (s), 639 (s), 576 (w), 519 (m), 475 (w) cm^{-1} . Anal. Calcd for $\text{C}_7\text{H}_4\text{F}_3\text{N}_3\text{O}_3\text{S}_3\text{Se}_2$: C, 17.18; H, 0.82; N, 8.59%. Found: C, 17.28; H, 1.08; N, 8.70%.

Preparation of 8-Chloro-4-methyl-4H-bis[1,2,3]selenathiazolo[4,5-b:5',4'-e]pyridin-2-iun Triflate, [**3a**][OTf]. Freshly prepared iodobenzene dichloride (2.52 g, 9.18 mmol) was added to a green slurry of [**3a**][OTf] ($\text{R}_1 = \text{Me}$, $\text{R}_2 = \text{H}$) (3.76 g, 7.68 mmol) in 400 mL of MeCN and the reaction was heated at reflux for 90 min. The solution was filtered hot through a fine (D porosity) frit, and the filtrate was concentrated to 250 mL. After leaving to stand for 16 h, the red precipitate of [**3a**][OTf] was filtered off and washed with 30 mL of DCM, yield 3.10 g (5.91 mmol, 77%). The solid was recrystallized from MeCN, dec >255 °C. IR: 1413 (m), 1352 (m), 1271 (m), 1237 (s), 1226 (s), 1198 (m), 1169 (m), 1153 (m), 1030 (s), 971 (w), 914 (w), 840 (m), 825 (m), 713 (s), 707 (m), 669 (m), 657 (s), 641 (s), 599 (w), 572 (w), 541 (w), 517 (m) cm^{-1} . Anal. Calcd for $\text{C}_7\text{H}_3\text{ClF}_3\text{N}_3\text{O}_3\text{S}_3\text{Se}_2$: C, 16.05; H, 0.58; N, 8.02%. Found: C, 16.32; H, 0.62; N, 8.20%.

Preparation of 8-Chloro-4-methyl-4H-bis[1,2,3]selenathiazolo[4,5-b:5',4'-e]pyridin-2-iun Nonaflate, [**3a**][ONf]. A solution of tetra-*n*-butylammonium bromide (1.96 g, 6.08 mmol) dissolved in 20 mL of MeCN was added to a hot solution of [**3a**][OTf] (2.12 g, 4.05 mmol) in 450 mL of MeCN. After 30 min the resulting green precipitate of [**3a**][Br] was filtered off and washed 3 × with 100 mL of MeCN, yield 1.80 g (3.96 mmol, 98%). IR: 1501 (w), 1415

(56) Brauer, G. *Handbook of Preparative Inorganic Chemistry*; Academic Press: New York, 1963; Vol. 1, p 423.

(s), 1403 (s), 1340 (s), 1201 (m), 1044 (m), 958 (w), 899 (w), 831 (m), 818 (m), 710 (m), 646 (s), 594 (w), 537 (w), 507 (m) cm^{-1} . Silver nonaflate (1.94 g, 4.76 mmol) was added to a slurry of [3a][Br] (1.80 g, 3.96 mmol) in 200 mL of MeCN to give a green solution that was warmed at 60 °C for 1 h. White AgBr was removed by double filtration on paper, and the filtrate was concentrated to 125 mL. After 2 h, the reaction mixture was cooled at -20 °C for 3 h, and the product [3a][ONf] was filtered off and rinsed with 20 mL of DCM, yield 2.47 g (3.66 mmol, 92%), dec >238 °C. IR: 1413 (m), 1351 (m), 1268 (m), 1234 (s), 1201 (m), 1179 (m), 1132 (m), 1059 (m), 1044 (m), 1018 (w), 1005 (w), 969 (w), 911 (w), 839 (m), 825 (m), 802 (w), 739 (w), 715 (s), 668 (m), 655 (s), 619 (w), 599 (w), 565 (w), 538 (w), 521 (w) cm^{-1} . Anal. Calcd for $\text{C}_{10}\text{H}_3\text{ClF}_9\text{N}_3\text{O}_3\text{S}_3\text{Se}_2$: C, 17.83; H, 0.45; N, 6.24%. Found: C, 18.08; H, 0.30; N, 6.52%.

Preparation of 8-Chloro-4-methyl-4H-bis[1,2,3]diselenazolo[4,5-b:5',4'-el]pyridin-2-iun Nonaflate, [4a][ONf]. Compound [3a][ONf] (0.675 g, 1.00 mmol) and finely ground selenium dioxide (0.340 g, 3.00 mmol) were combined with 80 mL of MeCN in a glass pressure vessel, which was then sealed and heated at 110 °C for 4 days. The heat was removed, and after 16 h the red solid of [4a][ONf] was filtered off and washed with 30 mL of DCM, yield 0.584 g (0.761 mmol, 76%). Recrystallization from MeCN afforded red flakes, dec >254 °C. IR: 1410 (m), 1343 (m), 1264 (m), 1230 (s), 1185 (m), 1147 (w), 1133 (m), 1058 (m), 1044 (w), 1027 (w), 1015 (w), 1002 (w), 959 (w), 847 (w), 804 (w), 756 (w), 738 (w), 705 (s), 659 (m), 638 (w), 619 (w), 579 (s), 534 (w), 522 (w) cm^{-1} . Anal. Calcd for $\text{C}_{10}\text{H}_3\text{ClF}_9\text{N}_3\text{O}_3\text{SSe}_4$: C, 15.65; H, 0.39; N, 5.47%. Found: C, 15.79; H, 0.28; N, 5.60%.

Preparation of Radicals 2a, 3a, 4a.

Method 1. Bulk Material for Conductivity and Magnetic Measurements of 2a and 3a. Degassed solutions (3 freeze-pump-thaw cycles) of [2a, 3a][OTf] (0.368–0.382 mmol) in 180–200 mL of MeCN and TMPDA (0.505–0.511 mmol) in 40 mL of MeCN were combined, and after 30 min the gold-brown precipitate of [2a, 3a] was filtered off and washed 5 × with 30 mL of MeCN and dried in vacuo.

Method 2. Diffusion H-Cells for Single-Crystal Growth of 2a and 3a. Degassed solutions (3 freeze-pump-thaw cycles) of HMFc (12 mg, 0.0444 mmol) in 8 mL of MeCN and [2a, 3a][OTf] (19 mg, 0.0363 mmol) in 15 mL of MeCN were allowed to diffuse together slowly at room temperature over a period of 16 h. The solvent was decanted to leave metallic green/black needles of 2a, 3a suitable for X-ray work.

Method 3. Electrococrystallization H-Cells for Single Crystal Growth of 4a. The electrococrystallization work employed standard electrochemical H-cell techniques,⁵⁷ with samples of [4a][ONf] (20 mg) dissolved under nitrogen in 20 mL of MeCN containing 0.025 M [n-Bu₄N][PF₆] as supporting electrolyte. Currents ranged from 5 to 10 μA , with growth periods of 2–4 days.

Analytical Data for Radicals 2a, 3a, 4a. Method 1, yield 0.125 g (0.334 mmol, 87%), dec >120 °C. IR: 1251 (m), 1184 (w), 1043 (m), 958 (m), 823 (w), 736 (m), 691 (m), 578 (m), 525 (m), 463 (w) cm^{-1} . Anal. Calcd for $\text{C}_6\text{H}_3\text{ClIN}_3\text{S}_2\text{Se}_2$: C, 19.24; H, 0.81; N, 11.22%. Found: C, 19.40; H, 0.90; N, 11.25%. 3a. Method 1, yield 0.103 g (0.274 mmol, 75%), dec >120 °C. IR: 1240 (s), 1192 (m), 1036 (m), 948 (w), 885 (w), 810 (w), 793 (m), 699 (m), 675 (s), 637 (s), 583 (m), 516 (m), 491 (m) cm^{-1} . Anal. Calcd for $\text{C}_6\text{H}_3\text{ClIN}_3\text{S}_2\text{Se}_2$: C, 19.24; H, 0.81; N, 11.22%. Found: C, 19.48; H, 1.02; N, 11.15%. 4a. Method 3, dec >120 °C. IR: 1247 (m), 1178 (m), 1029 (w), 934 (m), 692 (m), 684 (m), 567 (m), 557 (m), 526 (w), 435 (w) cm^{-1} . Anal. Calcd for $\text{C}_6\text{H}_3\text{ClIN}_3\text{Se}_4$: C, 15.39; H, 0.65; N, 8.97%. Found: C, 15.13; H, 0.81; N, 8.96%.

(57) (a) Ferraro, J. R.; Williams, J. M. *Introduction to Synthetic Electrical Conductors*; Academic Press: New York, 1987; p 25. (b) Stephens, D. A.; Rehan, A. E.; Compton, S. J.; Barkhau, R. A.; Williams, J. M. *Inorg. Synth.* **1986**, 24, 135.

X-ray Measurements. Needles of 2a, 3a and 4a were glued to glass fibers with epoxy. X-ray data were collected using omega scans with a Bruker APEX I CCD detector on a D8 3-circle goniometer and Mo K α ($\lambda = 0.71073 \text{ \AA}$) radiation or on a Bruker SMART APEX CCD-based diffractometer using Cu K α ($\lambda = 1.54178 \text{ \AA}$) radiation. The data were scanned using Bruker's SMART program and integrated using Bruker's SAINT software.⁵⁸ The structures were solved by direct methods using SHELXS-90⁵⁹ and refined by least-squares methods on F^2 using SHELXL-97⁶⁰ incorporated in the SHELXTL⁶¹ suite of programs.

Magnetic Susceptibility Measurements. DC magnetic susceptibility measurements on 2a, 3a and 4a were performed over the range 2–300 K on a Quantum Design MPMS SQUID magnetometer operating at $H = 100 \text{ Oe}$. Diamagnetic corrections were made using Pascal's constants,⁶² and the data were modeled using a molecular-field modified Heisenberg 1D AFM $S = 1/2$ chain fit function.⁶³

Ambient Pressure Conductivity Measurements. Four-probe temperature-dependent conductivity measurements were performed on pressed pellet samples using a Quantum Design PPMS instrument. Silver paint (Leitsilber 200) was used to apply the electrical contacts.

High-Pressure Conductivity Measurements. High-pressure conductivity versus temperature measurements on 2a and 4a were carried out in a cubic anvil press⁶⁴ using pyrophyllite ($\text{Al}_4\text{Si}_8\text{O}_{20}(\text{OH})_4$) as the pressure-transmitting medium. Sample pressure was determined from previous calibrations of the applied hydraulic load against pressures of structure transformations in standards at room temperature (Hg L \leftrightarrow I at 0.75 GPa, Bi I \leftrightarrow II at 2.46 GPa, Ti I \leftrightarrow III at 3.70 GPa, and Ba I \leftrightarrow II at 5.5 GPa).⁶⁵ Temperature was applied by Joulean heating of a cylindrical Nb foil (0.127 mm thick) furnace and monitored with a Pt/Pt + 10%Rh thermocouple, using a pressure-corrected emf.^{65,66} Two Pt electrodes contacted the precompacted, powder sample which was contained in a boron nitride ($\sigma_{BN} \approx 10^{-11} \text{ S cm}^{-1}$) cup. Four-wire ac (Solartron 1260 Impedance Analyzer) resistance measurements were made at a frequency of 1 kHz. Resistance was measured at temperature intervals of 5–8 °C over the range 25–90 °C on increasing/decreasing pressure over 5–6 h. The contiguous disk-shaped sample was extracted from the recovered pressure cell, and the sample geometry was measured to convert resistance to conductivity.

Band Structure Calculations. Band electronic structure calculations were performed with the CAESAR suite of programs⁶⁷ using the Coulomb parameters of Basch, Viste and Gray⁶⁸ and a quasi-split valence basis set adapted from Clementi and Roetti.⁶⁹ The off-diagonal elements of the Hamiltonian matrix were calculated with the standard weighting formula.⁷⁰ Atomic positions for the full 3D calculations were taken from crystallographic data. Coordinates for the model 1D-calculations of

- (58) SAINT, version 6.22; Bruker Advanced X-ray Solutions, Inc.: Madison, WI, 2001.
- (59) SHELXS-90: Sheldrick, G. M. *Acta Crystallogr., Sect. A* **1990**, 46, 467.
- (60) Sheldrick, G. M. *SHELXL-97. Program for the Refinement of Crystal Structures*; University of Göttingen: Göttingen, Germany, 1997.
- (61) SHELXTL, VERSION 6.12, *Program Library for Structure Solution and Molecular Graphics*; Bruker Advanced X-ray Solutions, Inc.: Madison, WI, 2001.
- (62) Carlin, R. L. *Magnetochemistry*; Springer-Verlag: New York, 1986.
- (63) Estes, W. E.; Gavel, D. P.; Hatfield, W. E.; Hodgson, D. J. *Inorg. Chem.* **1978**, 17, 1415.
- (64) Secco, R. A. *Can. J. Phys.* **1995**, 73, 287.
- (65) Secco, R. A.; Schloessin, H. H. *J. Appl. Phys.* **1986**, 60, 1625.
- (66) Bundy, F. P. *J. Appl. Phys.* **1961**, 32, 483.
- (67) CAESAR, Version 2 Program for Crystal and Electronic Structure Analysis; PrimeColor Software, Inc.: Cary, NC 1998.
- (68) Basch, H.; Viste, A.; Gray, H. B. *Theor. Chim. Acta* **1965**, 3, 458.
- (69) Clementi, E.; Roetti, C. *At. Data. Nucl. Data Tables* **1974**, 14, 177.
- (70) Ammeter, J. H.; Bürgi, H. B.; Thibeault, J. C.; Hoffmann, R. *J. Am. Chem. Soc.* **1978**, 100, 3686.

$\Delta E_k = [E_{(k=\pi/a)} - E_{(k=0)}]$ as a function of the stack slippage were performed using coordinates for **1–4** ($R_1 = R_2 = H$) taken from UB3LYP/6-31G(d,p) calculations optimized in C_{2v} symmetry; the interplanar separation along the π -stack was set at 3.5 Å. The smoothed energy surface was plotted from a grid consisting of at least 121 points.

Exchange Energy Calculations. All calculations were performed using the UB3LYP functional and the split-valence triple- ζ basis sets 6-31G(d,p) and 6-311G(d,p), as contained in the Gaussian 03W suite of programs.⁷¹ Exchange energies J_1 – J_4 and J_π for interacting pairs of radicals in **2a** and **4a** were computed from eq 1, using single-point energies of the lowest triplet and broken symmetry singlet states and their respective $\langle S^2 \rangle$ expectation values. Tight convergence criteria were employed, and atomic coordinates were taken from crystallographic data. Coordinates for the model 1D calculations of J_π as a function of the π -stack slippage (x, y) were performed using coordinates for **1–4** ($R_1 = R_2 = H$) taken from UB3LYP/6-31G(d,p) calculations optimized in C_{2v} ; the interplanar separation along the model π -stack was set at 3.5 Å. The smoothed energy surface was plotted from a grid consisting of at least 121 points.

(71) Frisch, M. J.; et al. *Gaussian 03, Revision C.02*; Gaussian, Inc.: Wallingford CT, 2004.

Acknowledgment. We thank the Natural Sciences and Engineering Research Council of Canada (NSERC) for financial support and for a Canada Graduate Scholarship to A.A.L. We also acknowledge the Canada Council for a Killam Research Fellowship to R.T.O.

Supporting Information Available: Complete authorship for references 3a, 13a and 71; ESI MS data for selenium insertion reactions, and X-ray powder diffraction patterns for chemically prepared **4a**; summaries of magnetic data fitting, DFT calculations of magnetic exchange interactions, and ΔE_k and J_π contour plots for **1–4** ($R_1 = R_2 = H$); details of X-ray crystallographic data collection and structure refinement, tables of atomic coordinates, bond distances and angles, anisotropic thermal parameters, and hydrogen atom positions in CIF format. This material is available free of charge via the Internet at <http://pubs.acs.org>.

JA900853T